# Detailed study of high-$p_T$ neutral pion suppression and azimuthal anisotropy in Au+Au collisions at $\sqrt{s_{NN}} = 200$ GeV

S. S. Adler,[5] S. Afanasiev,[17] C. Aidala,[5] N. N. Ajitanand,[43] Y. Akiba,[20,38] J. Alexander,[43] R. Amirikas,[12] L. Aphecetche,[45] S. H. Aronson,[5] R. Averbeck,[44] T. C. Awes,[35] R. Azmoun,[44] V. Babintsev,[15] A. Baldisseri,[10] K. N. Barish,[6] P. D. Barnes,[27] B. Bassalleck,[33] S. Bathe,[30] S. Batsouli,[9] V. Baublis,[37] A. Bazilevsky,[39,15] S. Belikov,[16,15] Y. Berndnikov ,[40] S. Bhagavatula,[16] J. G. Boissevain,[27] H. Borel,[10] S. Borenstein,[25] M. L. Brooks,[27] D. S. Brown,[34] N. Bruner,[33] D. Bucher,[30] H. Buesching,[30] V. Bumazhnov,[15] G. Bunce,[5,39] J. M. Burward-Hoy,[26,44] S. Butsyk,[44] X. Camard,[45] J.-S. Chai,[18] P. Chand,[4] W. C. Chang,[2] S. Chernichenko,[15] C. Y. Chi,[9] J. Chiba,[20] M. Chiu,[9] I. J. Choi,[52] J. Choi,[19] R. K. Choudhury,[4] T. Chujo,[5] V. Cianciolo,[35] Y. Cobigo,[10] B. A. Cole,[9] P. Constantin,[16] D. d'Enterria,[45] G. David,[5] H. Delagrange,[45] A. Denisov,[15] A. Deshpande,[39] E. J. Desmond,[5] A. Devismes,[44] O. Dietzsch,[41] O. Drapier,[25] A. Drees,[44] K. A. Drees,[5] R. du Rietz,[29] A. Durum,[15] D. Dutta,[4] Y. V. Efremenko,[35] K. El Chenawi,[49] A. Enokizono,[14] H. En'yo,[38,39] S. Esumi,[48] L. Ewell,[5] D. E. Fields,[33,39] F. Fleuret,[25] S. L. Fokin,[23] B. D. Fox,[39] Z. Fraenkel,[51] J. E. Frantz,[9] A. Franz,[5] A. D. Frawley,[12] S.-Y. Fung,[6] S. Garpman,[29,*] T. K. Ghosh,[49] A. Glenn,[46] G. Gogiberidze,[46] M. Gonin,[25] J. Gosset,[10] Y. Goto,[39] R. Granier de Cassagnac,[25] N. Grau,[16] S. V. Greene,[49] M. Grosse Perdekamp,[39] W. Guryn,[5] H.-Å. Gustafsson,[29] T. Hachiya,[14] J. S. Haggerty,[5] H. Hamagaki,[8] A. G. Hansen,[27] E. P. Hartouni,[26] M. Harvey,[5] R. Hayano,[8] N. Hayashi,[38] X. He,[13] M. Heffner,[26] T. K. Hemmick,[44] J. M. Heuser,[44] M. Hibino,[50] J. C. Hill,[16] W. Holzmann,[43] K. Homma,[14] B. Hong,[22] A. Hoover,[34] T. Ichihara,[38,39] V. V. Ikonnikov,[23] K. Imai,[24,38] D. Isenhower,[1] M. Ishihara,[38] M. Issah,[43] A. Isupov,[17] B. V. Jacak,[44] W. Y. Jang,[22] Y. Jeong,[19] J. Jia,[44] O. Jinnouchi,[38] B. M. Johnson,[5] S. C. Johnson,[26] K. S. Joo,[31] D. Jouan,[36] S. Kametani,[8,50] N. Kamihara,[47,38] J. H. Kang,[52] S. S. Kapoor,[4] K. Katou,[50] S. Kelly,[9] B. Khachaturov,[51] A. Khanzadeev,[37] J. Kikuchi,[50] D. H. Kim,[31] D. J. Kim,[52] D. W. Kim,[19] E. Kim,[42] G.-B. Kim,[25] H. J. Kim,[52] E. Kistenev,[5] A. Kiyomichi,[48] K. Kiyoyama,[32] C. Klein-Boesing,[30] H. Kobayashi,[38,39] L. Kochenda,[37] V. Kochetkov,[15] D. Koehler,[33] T. Kohama,[14] M. Kopytine,[44] D. Kotchetkov,[6] A. Kozlov,[51] P. J. Kroon,[5] C. H. Kuberg,[1,27,*] K. Kurita,[39] Y. Kuroki,[48] M. J. Kweon,[22] Y. Kwon,[52] G. S. Kyle,[34] R. Lacey,[43] V. Ladygin,[17] J. G. Lajoie,[16] A. Lebedev,[16,23] S. Leckey,[44] D. M. Lee,[27] S. Lee,[19] M. J. Leitch,[27] X. H. Li,[6] H. Lim,[42] A. Litvinenko,[17] M. X. Liu,[27] Y. Liu,[36] C. F. Maguire,[49] Y. I. Makdisi,[5] A. Malakhov,[17] V. I. Manko,[23] Y. Mao,[7,38] G. Martinez,[45] M. D. Marx,[44] H. Masui,[48] F. Matathias,[44] T. Matsumoto,[8,50] P. L. McGaughey,[27] E. Melnikov,[15] F. Messer,[44] Y. Miake,[48] J. Milan,[43] T. E. Miller,[49] A. Milov,[44,51] S. Mioduszewski,[5] R. E. Mischke,[27] G. C. Mishra,[13] J. T. Mitchell,[5] A. K. Mohanty,[4] D. P. Morrison,[5] J. M. Moss,[27] F. Mühlbacher,[44] D. Mukhopadhyay,[51] M. Muniruzzaman,[6] J. Murata,[38,39] S. Nagamiya,[20] J. L. Nagle,[9] T. Nakamura,[14] B. K. Nandi,[6] M. Nara,[48] J. Newby,[46] P. Nilsson,[29] A. S. Nyanin,[23] J. Nystrand,[29] E. O'Brien,[5] C. A. Ogilvie,[16] H. Ohnishi,[5,38] I. D. Ojha,[49,3] K. Okada,[38] M. Ono,[48] V. Onuchin,[15] A. Oskarsson,[29] I. Otterlund,[29] K. Oyama,[8] K. Ozawa,[8] D. Pal,[51] A. P. T. Palounek,[27] V. Pantuev,[44] V. Papavassiliou,[34] J. Park,[42] A. Parmar,[33] S. F. Pate,[34] T. Peitzmann,[30] J.-C. Peng,[27] V. Peresedov,[17] C. Pinkenburg,[5] R. P. Pisani,[5] F. Plasil,[35] M. L. Purschke,[5] A. K. Purwar,[44] J. Rak,[16] I. Ravinovich,[51] K. F. Read,[35,46] M. Reuter,[44] K. Reygers,[30] V. Riabov,[37,40] Y. Riabov,[37] G. Roche,[28] A. Romana,[25,*] M. Rosati,[16] P. Rosnet,[28] S. S. Ryu,[52] M. E. Sadler,[1] N. Saito,[38,39] T. Sakaguchi,[8,50] M. Sakai,[32] S. Sakai,[48] V. Samsonov,[37] L. Sanfratello,[33] R. Santo,[30] H. D. Sato,[24,38] S. Sato,[5,48] S. Sawada,[20] Y. Schutz,[45] V. Semenov,[15] R. Seto,[6] M. R. Shaw,[1,27] T. K. Shea,[5] T.-A. Shibata,[47,38] K. Shigaki,[14,20] T. Shiina,[27] C. L. Silva,[41] D. Silvermyr,[27,29] K. S. Sim,[22] C. P. Singh,[3] V. Singh,[3] M. Sivertz,[5] A. Soldatov,[15] R. A. Soltz,[26] W. E. Sondheim,[27] S. P. Sorensen,[46] I. V. Sourikova,[5] F. Staley,[10] P. W. Stankus,[35] E. Stenlund,[29] M. Stepanov,[34] A. Ster,[21] S. P. Stoll,[5] T. Sugitate,[14] J. P. Sullivan,[27] E. M. Takagui,[41] A. Taketani,[38,39] M. Tamai,[50] K. H. Tanaka,[20] Y. Tanaka,[32] K. Tanida,[38] M. J. Tannenbaum,[5] P. Tarján,[11] J. D. Tepe,[1,27] T. L. Thomas,[33] J. Tojo,[24,38] H. Torii,[24,38] R. S. Towell,[1] I. Tserruya,[51] H. Tsuruoka,[48] S. K. Tuli,[3] H. Tydesjö,[29] N. Tyurin,[15] H. W. van Hecke,[27] J. Velkovska,[5,44] M. Velkovsky,[44] V. Veszprémi,[11] L. Villatte,[46] A. A. Vinogradov,[23] M. A. Volkov,[23] E. Vznuzdaev,[37] X. R. Wang,[13] Y. Watanabe,[38,39] S. N. White,[5] F. K. Wohn,[16] C. L. Woody,[5] W. Xie,[6] Y. Yang,[7] A. Yanovich,[15] S. Yokkaichi,[38,39] G. R. Young,[35] I. E. Yushmanov,[23] W. A. Zajc,[9,†] C. Zhang,[9] S. Zhou,[7] S. J. Zhou,[51] and L. Zolin[17]

(PHENIX Collaboration)

[1]*Abilene Christian University, Abilene, Texas 79699, USA*
[2]*Institute of Physics, Academia Sinica, Taipei 11529, Taiwan*
[3]*Department of Physics, Banaras Hindu University, Varanasi 221005, India*
[4]*Bhabha Atomic Research Centre, Bombay 400 085, India*
[5]*Brookhaven National Laboratory, Upton, New York 11973-5000, USA*
[6]*University of California - Riverside, Riverside, California 92521, USA*
[7]*China Institute of Atomic Energy (CIAE), Beijing, People's Republic of China*
[8]*Center for Nuclear Study, Graduate School of Science, University of Tokyo, 7-3-1 Hongo, Bunkyo, Tokyo 113-0033, Japan*
[9]*Columbia University, New York, New York 10027 and Nevis Laboratories, Irvington, New York 10533, USA*
[10]*Dapnia, CEA Saclay, F-91191, Gif-sur-Yvette, France*
[11]*Debrecen University, H-4010 Debrecen, Egyetem tér 1, Hungary*
[12]*Florida State University, Tallahassee, Florida 32306, USA*
[13]*Georgia State University, Atlanta, Georgia 30303, USA*
[14]*Hiroshima University, Kagamiyama, Higashi-Hiroshima 739-8526, Japan*

[15]*Institute for High Energy Physics (IHEP), Protvino, Russia*
[16]*Iowa State University, Ames, Iowa 50011, USA*
[17]*Joint Institute for Nuclear Research, 141980 Dubna, Moscow Region, Russia*
[18]*KAERI, Cyclotron Application Laboratory, Seoul, South Korea*
[19]*Kangnung National University, Kangnung 210-702, South Korea*
[20]*KEK, High Energy Accelerator Research Organization, Tsukuba-shi, Ibaraki-ken 305-0801, Japan*
[21]*KFKI Research Institute for Particle and Nuclear Physics (RMKI), H-1525 Budapest 114, POBox 49, Hungary*
[22]*Korea University, Seoul, 136-701, Korea*
[23]*Russian Research Center "Kurchatov Institute," Moscow, Russia*
[24]*Kyoto University, Kyoto 606-8502, Japan*
[25]*Laboratoire Leprince-Ringuet, Ecole Polytechnique, CNRS-IN2P3, Route de Saclay, F-91128, Palaiseau, France*
[26]*Lawrence Livermore National Laboratory, Livermore, California 94550, USA*
[27]*Los Alamos National Laboratory, Los Alamos, New Mexico 87545, USA*
[28]*LPC, Université Blaise Pascal, CNRS-IN2P3, Clermont-Fd, 63177 Aubiere Cedex, France*
[29]*Department of Physics, Lund University, Box 118, SE-221 00 Lund, Sweden*
[30]*Institut für Kernphysik, University of Muenster, D-48149 Muenster, Germany*
[31]*Myongji University, Yongin, Kyonggido 449-728, Korea*
[32]*Nagasaki Institute of Applied Science, Nagasaki-shi, Nagasaki 851-0193, Japan*
[33]*University of New Mexico, Albuquerque, New Mexico 87131, USA*
[34]*New Mexico State University, Las Cruces, New Mexico 88003, USA*
[35]*Oak Ridge National Laboratory, Oak Ridge, Tennessee 37831, USA*
[36]*IPN-Orsay, Universite Paris Sud, CNRS-IN2P3, BP1, F-91406, Orsay, France*
[37]*PNPI, Petersburg Nuclear Physics Institute, Gatchina, Russia*
[38]*RIKEN (The Institute of Physical and Chemical Research), Wako, Saitama 351-0198, JAPAN*
[39]*RIKEN BNL Research Center, Brookhaven National Laboratory, Upton, New York 11973-5000, USA*
[40]*St. Petersburg State Technical University, St. Petersburg, Russia*
[41]*Universidade de São Paulo, Instituto de Física, Caixa Postal 66318, São Paulo CEP05315-970, Brazil*
[42]*System Electronics Laboratory, Seoul National University, Seoul, South Korea*
[43]*Chemistry Department, Stony Brook University, SUNY, Stony Brook, New York 11794-3400, USA*
[44]*Department of Physics and Astronomy, Stony Brook University, SUNY, Stony Brook, New York 11794, USA*
[45]*SUBATECH (Ecole des Mines de Nantes, CNRS-IN2P3, Université de Nantes) BP 20722 - 44307, Nantes, France*
[46]*University of Tennessee, Knoxville, Tennessee 37996, USA*
[47]*Department of Physics, Tokyo Institute of Technology, Tokyo, 152-8551, Japan*
[48]*Institute of Physics, University of Tsukuba, Tsukuba, Ibaraki 305, Japan*
[49]*Vanderbilt University, Nashville, Tennessee 37235, USA*
[50]*Waseda University, Advanced Research Institute for Science and Engineering, 17 Kikui-cho, Shinjuku-ku, Tokyo 162-0044, Japan*
[51]*Weizmann Institute, Rehovot 76100, Israel*
[52]*Yonsei University, IPAP, Seoul 120-749, Korea*

Measurements of neutral pion ($\pi^0$) production at midrapidity in $\sqrt{s_{NN}} = 200$ GeV Au+Au collisions as a function of transverse momentum, $p_T$, collision centrality, and angle with respect to reaction plane are presented. The data represent the final $\pi^0$ results from the PHENIX experiment for the first RHIC Au+Au run at design center-of-mass energy. They include additional data obtained using the PHENIX Level-2 trigger with more than a factor of 3 increase in statistics over previously published results for $p_T > 6$ GeV/$c$. We evaluate the suppression in the yield of high-$p_T$ $\pi^0$'s relative to pointlike scaling expectations using the nuclear modification factor $R_{AA}$. We present the $p_T$ dependence of $R_{AA}$ for nine bins in collision centrality. We separately integrate $R_{AA}$ over larger $p_T$ bins to show more precisely the centrality dependence of the high-$p_T$ suppression. We then evaluate the dependence of the high-$p_T$ suppression on the emission angle $\Delta\phi$ of the pions with respect to event reaction plane for seven bins in collision centrality. We show that the yields of high-$p_T$ $\pi^0$'s vary strongly with $\Delta\phi$, consistent with prior measurements [1,2]. We show that this variation persists in the most peripheral bin accessible in this analysis. For the peripheral bins we observe no suppression for neutral pions produced aligned with the reaction plane, whereas the yield of $\pi^0$'s produced perpendicular to the reaction plane is suppressed by a factor of $\sim$2. We analyze the combined centrality and $\Delta\phi$ dependence of the $\pi^0$ suppression in different $p_T$ bins using different possible descriptions of parton energy loss dependence on jet path-length averages to determine whether a single geometric picture can explain the observed suppression pattern.

## I. INTRODUCTION

High transverse momentum particles resulting from hard scatterings between incident partons have become one of the most effective tools for probing the properties of the medium created in ultra-relativistic heavy ion collisions at RHIC. Data from the four RHIC experiments have unequivocally established the phenomenon of high transverse momentum hadron suppression in Au+Au compared to (appropriately scaled) $p+p$ collisions [3–9], whereas the lack of similar suppression in $d$+Au collisions [9–12] provides strong evidence that the suppression is not due to modification of parton distributions in the incident nuclei. This suppression has been observed for a large variety of hadron species, at highest $p_T$ for $\pi^0$ and most recently $\eta$ [13], supporting further the notion that energy loss occurs at the parton level. Conversely, direct photon measurements by the PHENIX collaboration show that the yield of hard photons in Au+Au collisions is consistent with $p+p$ expectations scaled by the number of incoherent nucleon-nucleon collisions [14] and, thus, provide final confirmation that hard scattering processes occur at rates expected from pointlike processes. This observation makes definitive the conclusion that the suppression of high-$p_T$ hadron production in Au+Au collisions is a final-state effect. Measurements of azimuthal angle correlations between hadron pairs resulting from fragmentation of hard-scattered partons into jets have provided additional confirmation of final-state medium effects on these partons [15].

Predictions of high-$p_T$ suppression were made before the start of RHIC operation [16,17] and confirmation of these predictions may be considered one of the key successes of the RHIC program so far. The suppression of high-$p_T$ single hadrons was predicted to result from the energy loss of hard-scattered quarks and gluons in the hot and dense quantum chromodynamics (QCD) medium created in ultrarelativistic heavy-ion collisions (see Refs. [18,19] and references therein). In the canonical models, medium-induced gluon bremsstrahlung is expected to dominate the energy loss process [16], and calculations of the high-$p_T$ suppression factor incorporating this effect have been able to successfully describe the experimental measurements [20–22]; however, recent measurements of heavy quark suppression pose some questions to this canonical view. Nonetheless, from comparisons of the energy loss calculations with the experimental data, estimates of the initial net color charge density that is usually expressed in terms of a gluon rapidity density, $dN_g/dy$, have been obtained yielding $dN_g/dy \approx 1000$ and, assuming thermalization, estimates of the initial energy density have produced values in excess of $10 \, \text{GeV/fm}^3$ [23,24].

However, in spite of this success, there are still a number of outstanding issues with the interpretation of the Au+Au high-$p_T$ single-hadron suppression. Because the properties of the medium created in heavy-ion collisions are not *a priori* known, the energy-loss calculations necessarily use the observed suppression to infer initial parton densities,

usually through an intermediate parameter that appears in the energy loss calculations. Although the initial parton density obtained by such "tomographic" studies has to be consistent with the final (measured) total particle multiplicity, it is fair to acknowledge that the $p_T$ dependence of the suppression (rather than its absolute magnitude) is a more discriminating observable to test the various energy loss models. For $\pi^0$ spectra, the suppression in central Au+Au collisions at $\sqrt{s_{NN}} = 200$ GeV is found to be approximately constant with $p_T$ over the range, $3 < p_T < 10$ GeV/$c$. Although the different energy loss calculations can reproduce this $p_T$-independent suppression, the detailed explanation of the constancy is different in each model. The effects invoked to explain the $p_T$ dependence of the observed Au+Au high-$p_T$ suppression include finite-energy effects, absorption of energy from the medium, evolution from incoherent (Bethe-Heitler) to coherent (Landau-Pomeranchuk-Migdal or LPM) radiation with increasing parton energy [25], the $p_T$-dependent mixture of quark and gluon contributions to the hard-scattered parton spectrum, the increasingly larger exponent of the underlying (power-law) parton $p_T$ spectra [22], and shadowing/EMC effect [26]. Although most calculations of the high-$p_T$ suppression in Au+Au collisions account for shadowing/EMC modifications of the nuclear parton distributions and for the relative mixture of quarks and gluons in the hard-scattered parton spectra, finite-energy corrections, absorption of energy from the medium, and the description of the energy loss process itself differs from calculation to calculation. Clearly the central Au+Au single-particle spectra are not sufficient, by themselves, to validate or exclude any of the different energy loss models; we must use more "differential" probes of medium-induced energy loss to better understand the phenomenon.

A robust prediction of non-Abelian parton energy loss calculations is that the average energy loss as a function of the in-medium path length $L$ shows a quadratic dependence $\propto L^2$ [27]. Such a behavior predicted for a *static* QCD medium turns into an effective $\propto L$ dependence in an expanding quark-gluon plasma (QGP) [28]. In principle, the centrality dependence of the high-$p_T$ suppression [5,6,8] provides an effective test of energy-loss calculations because the length of the path of the partons in the medium will change between peripheral and central collisions. However, the energy loss calculations also have to account for changes in the initial properties of the medium with centrality and the extra flexibility in the description of the initial conditions means that the measured centrality dependence of the high-$p_T$ suppression also does not stringently constrain energy loss models [29]. However, the path length of the parton in the medium can also be controlled by selecting high-$p_T$ hadrons in different bins of azimuthal angle difference from the event-by-event determined reaction plane. Indeed, shortly after experimental observations of azimuthal anisotropy were reported [1,15], arguments were made that the high-$p_T$ anisotropy in noncentral collisions was due to the spatial asymmetry of the medium and the resulting $\Delta\phi$ dependence of parton path lengths [30,31]. However, recent analyses have argued that the large azimuthal anisotropies at high $p_T$ cannot be accounted for by energy loss alone—at least when realistic nuclear geometry is used to

_____

*Deceased.

†PHENIX Spokesperson: zajc@nevis.columbia.edu

describe the spatial asymmetry of the initial state [29,32,33]. Some of these analyses were based on a picture of the energy loss process in which quarks or gluons that have emitted radiation effectively disappear from the steeply falling high-$p_T$ spectrum because they are overwhelmed by partons of lower energy that escape from the medium losing little or no energy. In this picture, the medium effectively attenuates the high-$p_T$ quarks and gluons and the high-$p_T$ spectrum is dominated by partons originating near the surface—i.e., partons originating in the "corona" [29,32,33]. Then, the azimuthal anisotropy could be largely determined by the shape of the surface [32]. However, it has been separately argued that fluctuations in the number of emitted gluons may be large and such fluctuations may weaken the corona effect [28].

In this article we present measurements of $\pi^0$ production in $\sqrt{s_{NN}} = 200$ GeV Au+Au collisions from the PHENIX experiment at RHIC. These data, obtained during Run-2 operation of RHIC in 2002, include additional data obtained with the PHENIX Level-2 trigger, which improved the total statistics by a factor of $\sim$3 compared to the prior analysis in Ref. [6]. The analyses presented here have also benefited from advanced electromagnetic calorimeter calibrations and from improved understanding of the systematic errors in the $\pi^0$ measurement in course of the direct photon analysis presented in Ref. [14], where the $\pi^0$ decay photons provide the main source of background. With the improved statistics, the $p_T$ reach of the data is extended to higher $p_T$, allowing us to test whether the suppression starts to diminish above 10 GeV/$c$ in $p_T$. In addition, we extend the measurement of the centrality dependence of the suppression up to 8 GeV/$c$.

We present measurements of the dependence of the $\pi^0$ yield as a function of the angle $\Delta\phi$ of the $\pi^0$ with respect to the event reaction plane. By measuring the high-$p_T$ hadron suppression as a function of $\Delta\phi$, for a given centrality bin, we can keep the properties of the medium fixed and vary only the average geometry of the jet propagation in the medium. By comparing different centrality bins we can, in principle, test how the initial properties of the medium affect the induced energy loss. Traditionally, measurements of the $\Delta\phi$ dependence of hadron yields have been analyzed in terms of the azimuthal asymmetry parameter, $v_2$, and we note that the data presented here were used to obtain measurements of $\pi^0$ $v_2$ for comparison to inclusive photon $v_2$ [34]. However, in this publication we focus not on $v_2$, but explicitly on the suppression as a function of $\Delta\phi$, expressed in terms of the $\Delta\phi$-dependent nuclear modification factor $R_{AA}(\Delta\phi)$. Although the data presented this way contain, in principle, the same information as the combination of $\Delta\phi$-averaged $R_{AA}$ and $v_2$, $R_{AA}(\Delta\phi)$ provides a useful alternative way to evaluate the dependence of high-$p_T$ suppression on geometry because it effectively combines $R_{AA}(p_T)$ and $v_2$ into a single set of data. We analyze the combined $\Delta\phi$ and centrality dependence of the high-$p_T$ suppression in the context of different path-length and density dependencies of the parton energy loss process to evaluate whether any geometric picture can simultaneously describe the centrality and $\Delta\phi$ dependence of the observed high $p_T$ deficit.

## II. EXPERIMENTAL DETAILS

The data presented in this article were obtained during Run-2 operation of the PHENIX experiment [35] at the Relativistic Heavy Ion Collider facility at Brookhaven National Laboratory [36]. The primary detectors used to obtain the presented results were the PHENIX central arm spectrometers, particularly the electromagnetic calorimeters [37], and the two beam-beam counters (BBC's) [38]. In addition, the PHENIX zero-degree calorimeters [39] were used for triggering and centrality determination.

Two-photon decays of neutral pions were measured in the PHENIX electromagnetic calorimeter, located at a radial distance of $\sim$5.1 m from the beam-line, which has a pseudo-rapidity acceptance of $-0.35 < \eta < 0.35$ and covers $\pi$ radians in azimuth. The electromagnetic calorimeter is divided into eight sectors, with each sector covering the full pseudo-rapidity range and $\pi/8$ in azimuth. The calorimeter consists of two distinct parts using different technologies. A lead-scintillator sandwich calorimeter (PbSc) with 5 cm $\times$ 5 cm towers covers 3/4 (6 sectors) of the central arm acceptance. A lead-glass Čerenkov calorimeter (PbGl) with 4 cm $\times$ 4 cm towers covers the remaining 1/4 (2 sectors) of the central arm acceptance. The corresponding $\Delta\eta \times \Delta\phi$ acceptance of a single tower at $\eta = 0$ is $0.011^2$ and $0.0075^2$ for the PbSc and PbGl calorimeters, respectively.

The event reaction plane in Au+Au collisions was measured in the two BBC's. Each BBC consists of 64 hexagonal, quartz Čerenkov radiators closely packed around the beam pipe, in an approximately azimuthally symmetric configuration. The beam-beam counters, located 144 cm in each direction from the nominal center of the interaction diamond, are used to count charged particles produced in the pseudorapidity range $3.0 < |\eta| < 3.9$. The distribution of particles over the individual channels of the BBC's allows measurement of the azimuthal distribution, $dN_{ch}/d\phi$, of charged particles within this pseudorapidity acceptance. The BBC's also provide measurement of the collision vertex position along the interaction diamond with a resolution of 0.6 cm [38].

The data presented here were obtained using the PHENIX minimum-bias Level-1 trigger, based on the BBC's and the PHENIX zero-degree calorimeters, that selects $92.2^{+2.5}_{-3.0}\%$ of the total Au+Au hadronic interaction cross section of 6.9 b [6]. For a subset of the data, events selected by the Level-1 trigger were subjected to software Level-2 trigger filtering after full assembly of events in the PHENIX event builder [40]. A software algorithm performed a crude reconstruction of electromagnetic clusters by summing the pedestal-subtracted and gain-calibrated energies of "tiles" made of adjacent 4 × 4 calorimeter towers groups. The tiles are allowed to overlap such that every possible such tile that can be constructed in each calorimeter is tested. One of the Level-2 triggers (LVL2A) selected events in which at least one cluster (tile) had energy >3.5 GeV. Another Level-2 trigger (LVL2B) selected events in the 50–92% centrality range (50% most peripheral events) with at least one cluster having energy >1.5 GeV.

The measurements presented in this article were obtained from 31.4 M minimum bias triggers and approximately

1.7 M Level-2 trigger selected events. Of the Level-2 triggered events, 743 K events were selected by the higher energy LVL2A trigger and the remainder were selected by the peripheral, lower-energy LVL2B trigger. Taking into account their rejection factors, the two triggers sampled the equivalent of $44.4 \times 10^6$ LVL2A and $28.7 \times 10^6$ LVL2B minimum-bias triggers. The difference is due to different online trigger pre-scale factors. Thus, the combined event sample contains approximately a factor of 2.5–3 (considering both triggers over all centralities) more $\pi^0$'s above 6 GeV/$c$ than previously published Run-2 $\pi^0$ measurements [6].

## III. DATA ANALYSIS

### A. Event selection and centrality

In the offline analysis, the timing difference measured between the two PHENIX BBC's is used to determine the position of the collision vertex along the beam axis and to select events with vertex position within 30 cm of the nominal center of the detector for subsequent analysis. The energies measured in the zero-degree calorimeters and the charged-particle multiplicity measured in the BBC's are used to determine the collision centrality [41]. For the $\pi^0$ spectrum measurements presented here the total measured centrality range (0–92.2%) is subdivided into nine bins: 0–10, 10–20, 20–30, 30–40, 40–50, 60–70, 70–80, 80–92.2%. For the reaction plane-dependent analysis, the most central and two most peripheral bins are excluded, the peripheral due to their large uncertainty in the reaction plane resolution, and the 0–10% bin simply because of its smaller intrinsic eccentricity. Additionally, we present also combined 0–20%, 20–60%, and 60–92% data sets for comparison with other PHENIX analyses of high $p_T$ hadron production that use such centralities.

### B. Reaction plane measurement

PHENIX has previously published measurements of elliptic flow using an event-by-event measured reaction plane [34,42, 43], and the same technique is used for the analysis presented here. Each BBC detector consists of 128 quartz radiators placed in hexagonal, roughly concentric rings whose light is individually collected by photomultiplier tubes (PMT's). The calibrated charge from each radiator is converted into an estimate for the number of charged particles within the acceptance of each detector, $N_i$, using the measured single-particle peak centroid.

For the reaction plane measurement the measured $N_i$ values are corrected such that the weight of the inner rings that have the fewest radiators covering the full azimuthal angle range is reduced. Then, in terms of the corrected $N_i$ values, $N_i^{\text{adj}}$, the angle of the reaction plane $\Psi$ is obtained from the formula

$$\tan(2\Psi) = \frac{\sum_i N_i^{\text{adj}} \sin(2\phi_i) - \left\langle \sum_i N_i^{\text{adj}} \sin(2\phi_i) \right\rangle}{\sum_i N_i^{\text{adj}} \cos(2\phi_i) - \left\langle \sum_i N_i^{\text{adj}} \cos(2\phi_i) \right\rangle}, \quad (1)$$

where $\phi_i$ represents the azimuthal angle of the center of a given radiator $i$. The subtraction of the average centroid position in Eq. (1) removes the bias in the reaction plane

TABLE I. Relative systematic uncertainty of the reaction plane resolution for the centrality bins shown in Fig. 1.

| Centrality | Syst. error |
|------------|-------------|
| 0–10%      | 20.3%       |
| 10–20%     | 5.1%        |
| 20–30%     | 3.9%        |
| 30–40%     | 3.8%        |
| 40–50%     | 4.1%        |
| 50–60%     | 4.6%        |
| 60–70%     | 22.5%       |

measurement resulting from nonzero angle of the colliding beams, nonuniformities in detector acceptance, and other similar effects. The average is taken over many events localized in time with the event in question. A final correction is applied to remove nonuniformities at the 20% level in the $\Psi$ distribution.

Because the above-described procedure can also be applied individually to each BBC, we have a redundant measurement of the reaction plane in the north and in the south, and we exploit this to determine the resolution of the full reaction plane measurement using standard procedures [44]. The resolution of the reaction plane is directly measured from the quantity $\langle \cos 2(\Psi_1 - \Psi_2) \rangle$ where $\Psi_1$ and $\Psi_2$ are the reaction plane angles measured in each of the two beam-beam counters individually and the average is taken over events. Figure 1 and Table I show the variation of the resolution, usually determined as $\langle \cos 2(\Psi_{\text{meas}} - \Psi_{\text{true}}) \rangle = \sqrt{(2\langle \cos 2(\Psi_1 - \Psi_2) \rangle)}$. The needed correction factors can be derived from this using Eq. (11) in Sec. III F, where the reaction plane corrections are described in more detail.

The systematic errors associated with the measurement of the reaction plane come dominantly from how well the resolution is known. The uncertainty on this quantity is also shown with Fig. 1 for all but the most peripheral centralities. This error is determined by observing comparison of the
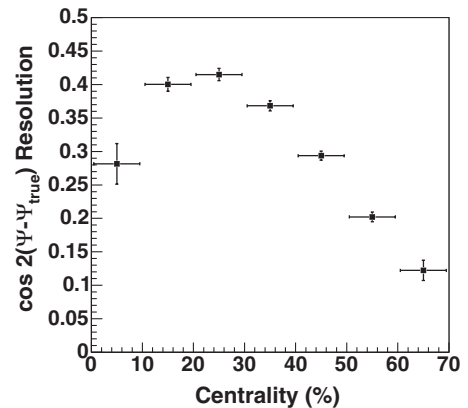


FIG. 1. Resolution of the reaction plane determined in the BBC versus centrality. As usual, the resolution is defined as the unitless quantity $\langle \cos 2(\Psi_{\text{meas}} - \Psi_{\text{true}}) \rangle$, equal to the inverse of the $v_2$ correction factor.

similarly calculated quantity $\langle \sin 2(\Psi_1 - \Psi_2) \rangle$ which should by definition be equal to zero. The value of $\langle \sin 2(\Psi_1 - \Psi_2) \rangle$ is found to be consistent with 0 for all centralities. The mean size of its fluctuations around 0 are compared to the size of the $\langle \cos 2(\Psi_1 - \Psi_2) \rangle$ to derive the systematic errors in the table. Because the value of $\langle \cos 2(\Psi_1 - \Psi_2) \rangle$ decreases dramatically in the lower multiplicity peripheral events, the relative size of the error increases. The size of this relative error is also cross checked by comparing it to the relative error on elliptic flow ($v_2$) measurements which is directly comparable since, as discussed in Sec. III F, the resolution correction for $v_2$ is a plain multiplicative factor. For the cross check, the $v_2$ error is derived by taking the difference of $v_2$ made with reaction planes from the BBC North and BBC South separately.

Because of the large rapidity gap between the PHENIX BBC's and the PHENIX Central Arm ($\Delta \eta > 2.7 - 4.0$), the measurements made in the BBC's are assumed to have no correlations (except collision geometry) with processes detected in the central arm that would affect the results presented in Sec. III F. Specifically, PYTHIA studies [45] indicate that any large rapidity-gap production correlated with jets (and thus the hard $\pi^0$'s we study) detected in the central arm have a negligible effect on reaction plane determination even for the most peripheral events considered in this article. Further, we average both the North and South BBC, which are separated by $\Delta \eta > 6.0$, making potential effects of this nature especially unlikely.

## C. Neutral pion detection

The detection of neutral pions is one of the major sources of information on identified particle production at high $p_T$ at RHIC, and PHENIX has already published the results of a number of $\pi^0$ measurements in different colliding systems [3,6,10,46,47]. Here we will describe the technique for obtaining $\pi^0$ yields as a function of $p_T$ and centrality, which is now well established within PHENIX.

Neutral pions are detected via their $\pi^0 \rightarrow \gamma + \gamma$ decay channel. Due to the relatively short mean lifetime of neutral pions of about $10^{-16}$ s, typical of electromagnetic decays, the pions decay close to the interaction point ($c\tau \approx 25$ nm). This makes the decay vertex well known and the pions can be reconstructed via an invariant mass analysis of photon pairs measured by the EMCal.

In the EMCal, hits or clusters are reconstructed by finding contiguous calorimeter towers with pulse heights above the ADC pedestal value. In order to obtain a cleaner sample of electromagnetic hits shower shape cuts are applied to select candidate photons and time-of-flight cuts are applied to reject slow hadrons. For the PbSc we require measured cluster times to be $t_{\text{clust}} < L/c \pm 1.2$ ns, where $L$ is the straight-line path from the collision vertex to the reconstructed cluster centroid. For the PbGl we require reconstructed clusters to have times, $t_{\text{clust}} < L/c \pm 2$ ns; the difference is due to the intrinsic timing resolutions of the two calorimeter technologies.

The energy of each EMCal cluster is corrected for angular dependence and nonlinearity based on test beam results and simulation. The linearity corrections for both detector types

are different with the PbGl showing a stronger dependence on the energy. The correction factors for a photon with a detected energy of 1 GeV (10 GeV) are 1 (0.95) for the PbSc and 1.05 (0.975) for the PbGl, respectively. The PbGl calorimeter also shows a stronger variation of the measured photon energy with the angle of incidence on the detector surface, at $20°$ the measured energy is reduced by 5% compared to perpendicular incidence ($0°$), whereas in the PbSc the effect is only of the order of 2%.

In a typical Au+Au central event the EMCal detects $\gtrsim 300$ clusters corresponding to an occupancy of $\sim 10\%$ and therefore a non-negligible probability of cluster overlaps. To minimize the effects of cluster overlaps in high multiplicity events, the energy of each cluster in the PbSc calorimeter is determined not only from the sum of all contiguous towers with deposited energy above a given threshold (15 MeV was our default value) but also, alternatively, "extrapolating" the measured "core energy" of the four to five central towers assuming a standard electromagnetic shower profile in an event with zero background. For this latter case, the *ecore* energy was computed from the experimentally measured center of gravity, central shower energy, and impact angle in the calorimeter using a parameterized shower profile function obtained from electromagnetic showers measured in the beam tests. Such an *ecore* energy represented an estimate of the true energy of a photon impinging on the PbSc unbiased by background contributions from other particles produced in the same event and depositing energy in the neighborhood of a given cluster. The use of *ecore* instead of the total cluster energy for photon reconstruction, helped to reduce considerably the effects of cluster overlaps in central Au+Au collisions.

For a photon pair originating from a $\pi^0$ decay the invariant mass

$$m_{\gamma\gamma} = \sqrt{\left(P_{\gamma_1} + P_{\gamma_2}\right)^2} = \sqrt{2E_1 \cdot E_2 \cdot (1 - \cos\theta_{12})} \qquad (2)$$

is identical to the $\pi^0$ rest mass. However, due to the finite energy and position resolution in the detection of the photon pair, the actual reconstructed value is smeared around a mean value, which can deviate from the nominal value. The reconstructed peak position is also influenced by the high multiplicity in a heavy-ion collision, where overlapping clusters can shift the measured energy of each photon.

With the invariant mass analysis, $\pi^0$'s cannot be identified uniquely because all possible photon-photon combinations have to be considered. This leads to a large combinatorial background, which increases quadratically with the multiplicity. The $\pi^0$ yield is instead determined on a statistical basis, with the background contribution established via a *mixed event* technique as described below.

One possibility to reduce the combinatorial background is to make use of the phase-space distribution of the photons in a $\pi^0$ decay. For the $\pi^0 \rightarrow \gamma + \gamma$ decay, the two photons have minimum opening angle

$$\tan\theta_{12}/2 = \frac{m}{p}, \qquad (3)$$

where $m$ is the $\pi^0$ mass and $p$ its momentum, with $p \simeq p_T$ in the PHENIX central spectrometer. The angular distribution of
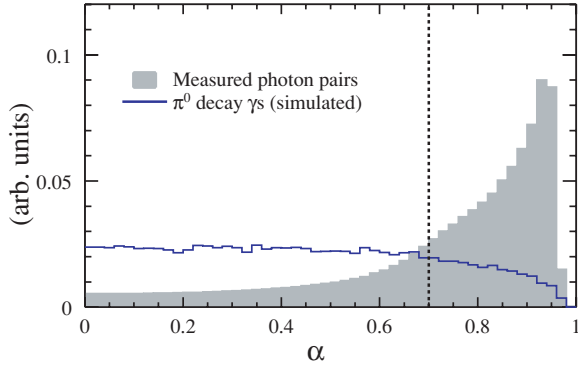
FIG. 2. (Color online) Asymmetry of photon pairs with $3\,\text{GeV}/c \leqslant p_T < 5\,\text{GeV}/c$ within the acceptance of one PbGl sector, for simulated single $\pi^0$s and measured within minimum bias events. An asymmetry cut used during the analysis is also shown. (Due to the limited acceptance of the detector, the distribution of the energy asymmetry shows a slight decrease toward $\alpha = 1$.)

the $\gamma$ pair in the $\pi^0$ rest frame, $d\sigma/d\cos\theta^*$, is constant, which leads to a flat distribution in the measured energy asymmetry of the two photons from $\pi^0$ decay:

$$\alpha = \frac{|E_1 - E_2|}{E_1 + E_2} = \beta|\cos\theta^*|, \qquad (4)$$

where $\beta = p/E \sim 1$ is the velocity of the $\pi^0$. However, high $p_T$ combinatorial pairs are strongly peaked near $\alpha = 1$ because of the steeply falling spectrum of single photon candidates. This is illustrated in Fig. 2, where the asymmetry distribution for photons from $\pi^0$s in a simulation is compared to the measured asymmetry for photon candidate pairs in real Au+Au collisions. In two independent analyses, asymmetry cuts of $\alpha < 0.7$ and $\alpha < 0.8$ were employed, other values were used as a cross-check and to verify the energy scale (see below).

Pairs of candidate photon clusters within the PbGl and the PbSc calorimeter that satisfy the asymmetry cut are considered candidate $\pi^0$'s. Figure 3 shows example invariant mass distributions for $\pi^0$ candidates with $3.0 < p_T < 3.5$ GeV/$c$ in Au+Au collisions for two different bins of collision centrality. The background under the clear $\pi^0$ mass peak in these figures is due to combinatorial mixing of photons from two different decaying $\pi^0$'s or from pairs containing one or two nonphoton clusters that nonetheless pass the above-described cuts.

Such a combinatorial background can be determined by a so-called *mixed event* technique. It is a widely used method to determine the combinatorial background of combined particle properties, e.g., the invariant mass of a photon pair. The basic idea is to compare the result obtained by combining particles within one event to the result for particle combinations from different events, which are *a priori* not correlated.
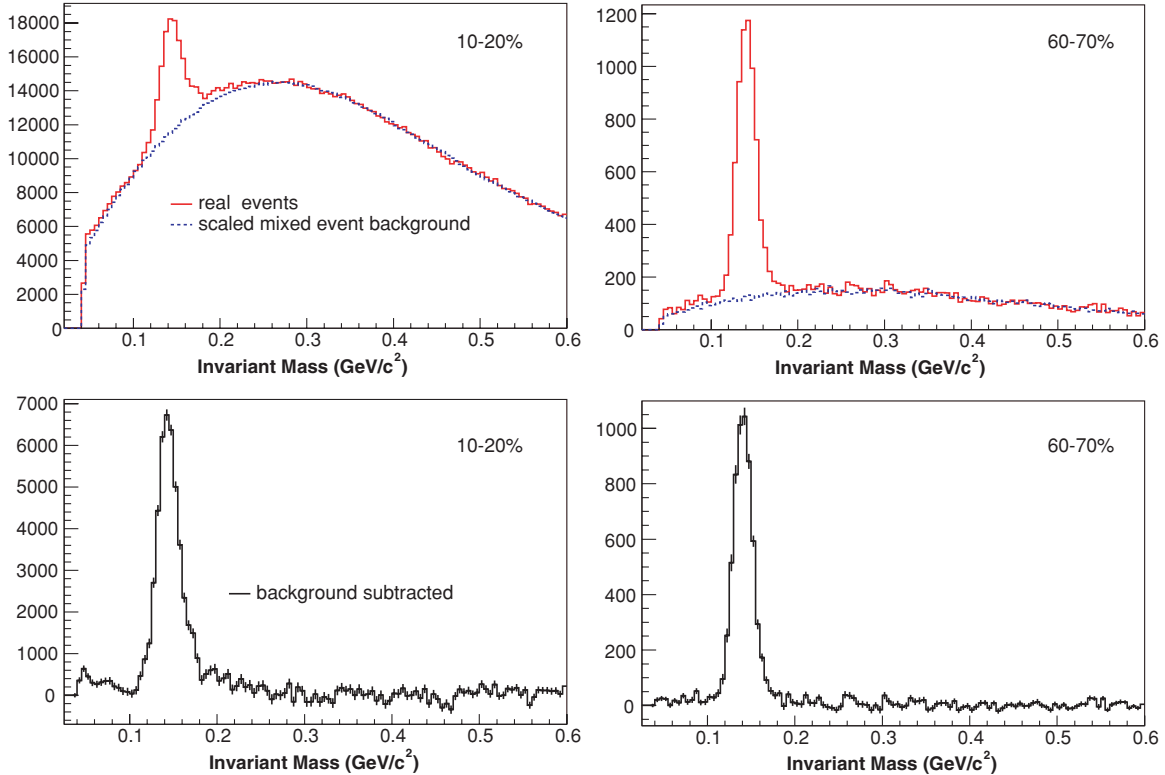


FIG. 3. (Color online) Invariant mass distributions of pairs of electromagnetic clusters passing photon selection cuts for pair transverse momenta satisfying $3.0 < p_T < 3.5$ GeV/$c$. (Top panels) $m_{\gamma\gamma}$ distributions in Au+Au events compared to a normalized mixed-event sample representing the combinatoric background. (Bottom panels) The $m_{\gamma\gamma}$ distributions after subtraction of the combinatoric background. (Left) 10–20% centrality bin; (right) 60–70% centrality bin.

In the case of the $\pi^0$ invariant mass, the mixed event distribution is determined by combining one photon candidate from the current event with all photon candidates from previous events stored in a buffer. The number of previous events used for the pair combinations determines the statistical error of the background, which can be made small by increasing the buffer size. In this analysis, the buffer is varied from $\sim$3 to 10 previous events depending on centrality due to the centrality-dependent multiplicity.

To describe the combinatorial background correctly it is essential that the events used for mixing have similar properties as the real event. Different event classes for collision vertex, centrality, and reaction plane are employed. Also events are chosen for mixing so that they are not biased toward a certain reaction. This is because triggered samples, even from the high-$p_T$ photon trigger, contain biases, e.g., in momenta and centrality distributions, which do not accurately represent the dominant uncorrelated background. For this reason only minimum bias events are used for mixing with both the trigger and minimum bias data sets.

For the photons used in the event mixing the same criteria are applied as for the pair combinations from one event, such as PID cuts, cuts on bad modules, and the asymmetry cut. Other properties valid *a priori* for the real photon pairs, e.g., a minimum distance that allows to distinguish them, have to be considered in addition. In the analysis a minimum distance cut of a least 8 cm is required for each photon pair combination, within one event and for mixed events, respectively.

For a given $p_T$ bin the mixed-event background is normalized to the same-event invariant mass distribution outside the range of the $\pi^0$ peak by scaling the mixed-event background with a function $f(m_{\mathrm{inv}})$. This scaling function is determined by fitting the ratio of the same-event and mixed-event invariant mass distribution for $p_T$ bins up to 3 GeV/$c$ with a linear function. This is needed because at low $p_T$ correlations in the real-event background due to overlapping clusters cannot be reproduced by the mixed-event technique. For the $p_T$ bins above 3 GeV/$c$, a constant is used. To cross-check the result, the linear and the constant scaling function are also determined over the complete invariant mass region, including the $\pi^0$ peak, which is taken into account by an additional Gaussian in the fit function (e.g., a linear plus a Gaussian function).

The determination of the scaling function for large pair-$p_T$ is limited by statistics in the real event sample and does not lead to stable results. Instead a constant scaling factor is used if the ratio of the invariant mass distribution shows bins with zero entries in the fit region. The scaling factor is determined by integrating the real and the mixed invariant mass distributions in the range with the peak region excluded.

The scaled mixed-event background is subtracted from the same-event distribution to produce a statistical measure of the true $\pi^0$ yield. The result of such a subtraction procedure is shown in the bottom plots of Fig. 3. The raw $\pi^0$ yield is obtained in each $p_T$ bin by integrating the subtracted invariant mass distribution in a range around the peak mean ($m_{\pi^0}$) of $\pm 3$ times the Gaussian width ($\sigma_{\pi^0}$) of the $\pi^0$ peak. Values of the mean and $\sigma_{\pi^0}$, can be seen in Fig. 4. Varying the size
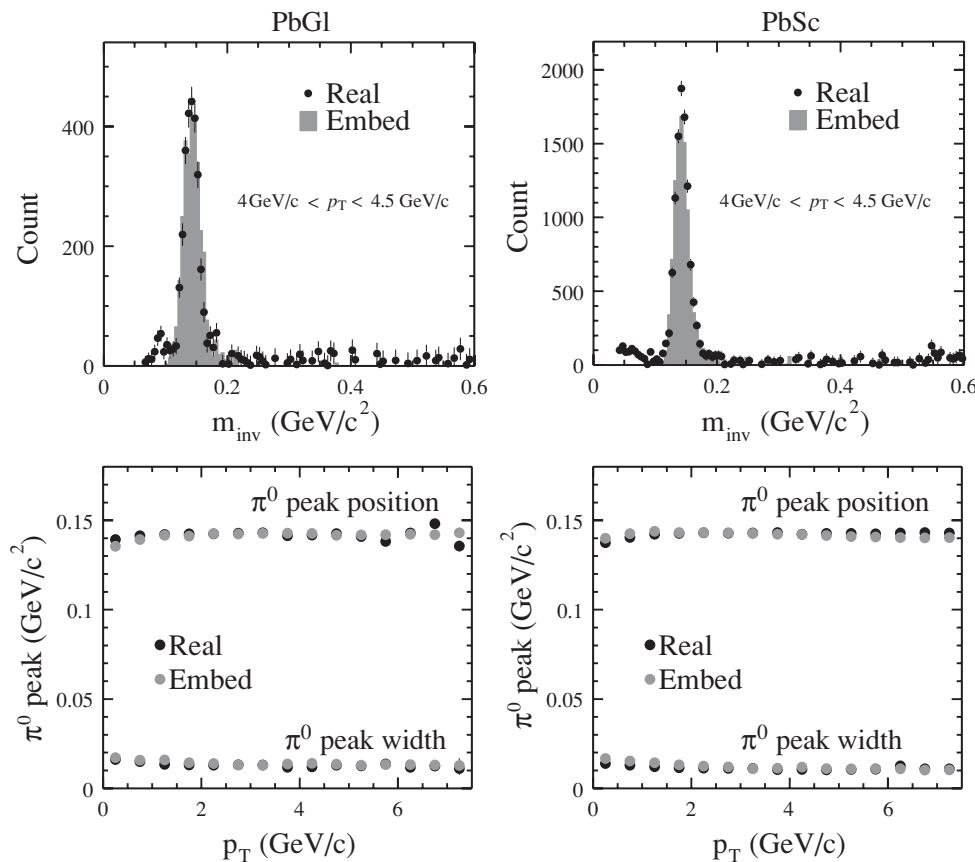


FIG. 4. Comparison of the $\pi^0$ peak position in real events (MB) measured with the PbGl and the PbSc with the results obtained for embedded $\pi^0$s. The $p_T$ dependence of the peak position and width is due to calorimeter energy resolution as discussed in the text.

of the integration window results in slightly different results, which contributes to the overall systematic uncertainty of the measurement, discussed in Sec. III D4.

Residual differences between the mixed background and the foreground are still apparent in some $p_T$ bins, especially below ∼2 GeV/$c$. Cluster merging, cluster splitting (fluctuations in the two-dimensional $\phi - z$ energy profile cause multiple local maxima that are incorrectly separated into distinct clusters), antineutron annihilation, and even second-order residual physics correlations such as three and multibody decays, flow, HBT, etc., can all cause such differences. These remaining differences are compensated by the shape of the scaling function. In addition, as a systematic check, the shape of the remaining background after subtraction is also fit with various low order polynomial functions and potential contributions to the peak yield are considered in the determination of the total systematic error from the peak extraction procedure.

The values of the peak width and mean are extracted in one initial analysis of the invariant mass distribution in which a $p_T$-dependent parameterization is determined for different centralities. The use of predefined values for the position and spread of the $\pi^0$ peak has the advantage that even in $p_T$ regions where no fit to the subtracted invariant mass distribution is possible, the integration region is well defined just by extrapolation from low $p_T$.

### D. $\pi^0$ spectrum measurement

For the reaction-plane independent $\pi^0$ spectrum measurement in a given centrality class *cent*, the aforementioned analysis is applied in $\Delta p_T = 0.5$ GeV/$c$ bins for $p_T > 1$ GeV/$c$. We cease attempting to extract $\pi^0$ yields at high $p_T$ when the number of pairs within the selected (background-subtracted) $\pi^0$ mass window falls below 4 counts. We then correct the resulting raw $\pi^0$ spectrum for the geometric acceptance $a_{\Delta y}(p_T)$, the overall detection efficiency $\varepsilon_{\mathrm{cent}}(p_T)$, which accounts for the cluster cut efficiency, the $\pi^0$ mass cut efficiency, for losses due to cluster overlaps in high multiplicity events, for cuts on bad modules and for the calorimeter energy and position resolution. In addition a correction for conversion losses ($c_{\mathrm{conv}}$) in the material of the PHENIX central arms and for the branching ratio of the two photon decay ($c_{\gamma\gamma}$) is applied:

$$\frac{1}{2\pi p_T} \frac{d^2 N_{\mathrm{cent}}^{\pi^0}}{dp_T\, dy} \equiv \frac{1}{2\pi p_T N_{\mathrm{cent}}^{\mathrm{event}}} \times \frac{1}{a_{\Delta y}(p_T)\varepsilon_{\mathrm{cent}}(p_T)c_{\mathrm{conv}}c_{\gamma\gamma}}$$
$$\times \frac{N_{\mathrm{cent}}^{\pi^0}(\Delta p_T)}{\Delta p_T\, \Delta y}. \tag{5}$$

#### 1. Acceptance and detector efficiency

The geometric acceptance of the EMCal for the $\pi^0 \to \gamma\gamma$ decay is evaluated using a Monte Carlo (MC) program that generates $\pi^0$s in a rapidity interval $\Delta y$ with the same vertex distribution and rapidity distribution as observed in real events and contains the complete geometry information of the EMCal. The $\pi^0$ decay is calculated via JETSET routines that are part of the PYTHIA event generator [48]. For each $\pi^0$

it is verified that both decay photons hit the detector. The resulting $p_T$ distribution of accepted $\pi^0$s is divided by the transverse-momentum distribution of the generated $\pi^0$s and provides the geometrical acceptance of the PbSc and PbGl, respectively.

The detection efficiency is determined using GEANT to simulate the complete response of the calorimeter to single $\pi^0$ decays. The data from each simulated $\pi^0$ is then embedded into real Au+Au events by adding the EMCal tower information of the simulated $\pi^0$ to the tower information of the real event and recalculating the EMCal clusters. The efficiency for detecting the embedded $\pi^0$ is then again determined by comparing the input $p_T$ spectrum to the reconstructed $p_T$ spectrum of the embedded $\pi^0$'s. Using this technique we determine "efficiency" corrections that account for the energy resolution and position resolution of the calorimeter, as well as for the losses due to overlapping clusters in a real event environment. In addition, the embedding allows for a precise determination of the effect of edge cuts and bad modules. Though these effects can be in principle considered as acceptance corrections, they depend not only on the geometry but also on the energy deposition of an electromagnetic shower in the different calorimeter towers.

In the embedding procedure the effects of photon conversions are also included, as the GEANT simulation considers the material budget in front of the EMCal and the information for decay-photon conversions is retained. The final conversion correction, which is factorized from the rest of the efficiency for book-keeping purposes, is evaluated by comparing the $\pi^0$ yield with and without including conversions in the simulation. The final conversion correction, constant with $p_T$ depends on the photon PID cuts and material in front of each individual sector and ranges from 6 to 8% in PbGl and 9 to 10% in PbSc. Comparing this to the sheer probability of a $\pi^0$ having at least one photon which converts, 21% PbGl and 14% PbSc, we see that a large portion of these $\pi^0$ are still reconstructable.

For the embedding, the input $\pi^0$ spectrum is weighted to match a fit function (see below, at the end of Sec. III D3) which is fit to the measured $\pi^0$ spectrum so that the correct folding of the $\pi^0$ spectrum with the resolution is obtained. This procedure is iterated, with the fit of the $p_T$ dependence of the input weights adjusted as the estimate of the efficiency correction improves, until the procedure converges within the nearly $p_T$-independent statistical error of the embedded sample, approximately 3%.

Figure 4 compares the invariant-mass peak after background subtraction in the real data and the invariant mass peak of the embedded $\pi^0$ for the two different detector types in minimum bias events. The measured $\pi^0$ peak position is shifted from the nominal value of approximately 134.98 MeV due to the finite energy resolution of the detector in combination with the steeply falling spectrum and due to the additional effect of overlapping clusters. As illustrated the effects are well reproduced by the embedded $\pi^0$'s.

#### 2. Trigger efficiency

The efficiency of the Level-2 trigger is separately evaluated by processing recorded minimum-bias events with the Level-2
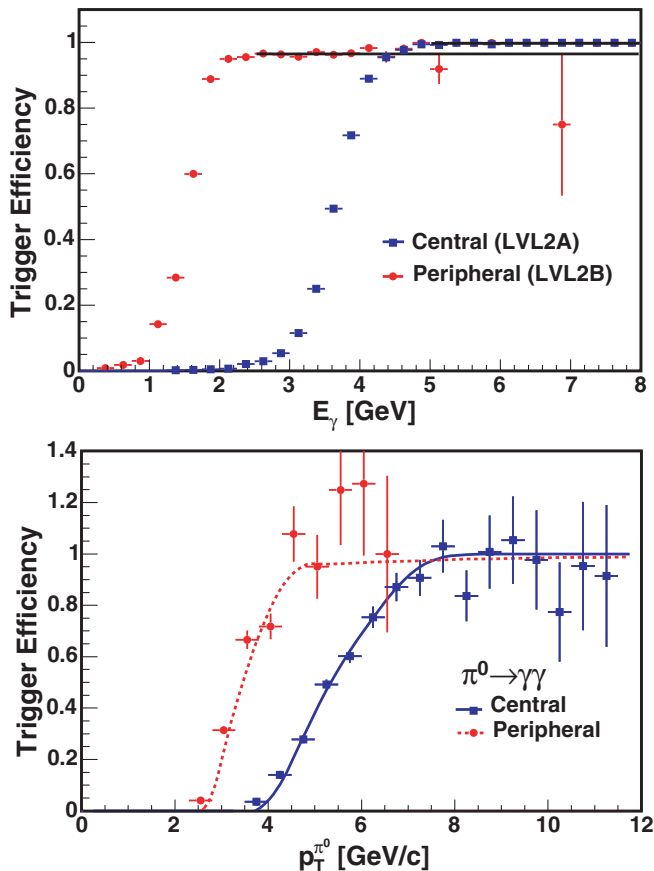
FIG. 5. (Color online) (Upper) Measured efficiency of single clusters of LVL2A (blue) and LVL2B (red) triggers as discussed in the text. The black lines are constant value fits to the plateau efficiency, greater than 99.7 (95%) for LVL2A (LVL2B). (Lower) Efficiency for neutral pion detection of the triggers as a function of $\pi^0$ $p_T$, calculated (solid curves) based on the efficiencies in (upper) and, as a cross-check (data points), compared to ratio of per equivalent minimum-bias event yields in the full trigger sample with the same in the true minimum bias sample. Because the latter is the ratio of two separate data samples, independent statistical fluctuations, as well as $\sim$8% systematic effects in the yield extraction (discussed Sec. III D4) in either sample can cause this measured ratio to be greater than 100%.

trigger and evaluating the efficiency for the trigger to select events containing a high $p_T$ cluster. This analysis shows complete (100%) efficiency for the LVL2A trigger at momenta well above the trigger threshold of 3.5 GeV/$c$ (95% above 1.5 GeV/$c$ for LVL2B) for obtaining clusters that also pass all offline cluster cuts. This is demonstrated in Fig. 5 (upper). The "plateau" values are determined from fitting the region above the turn-on also shown.

The related trigger efficiency of reconstructed $\pi^0$'s is calculated from a fast MC simulation based on these measured single cluster efficiencies. The calculation is performed both by using a integrated Gaussian fit to the single cluster efficiency and by directly using the finely binned histogram and constant plateau fit. Both methods give consistent results. The result for the latter method is shown in Fig. 5 (lower), solid curves. The calculation is cross-checked, as demonstrated by the data

TABLE II. Corrections in the PbGl and PbSc to the raw $\pi^0$ yield in central collisions (0–10%) and with TOF and shower shape cut applied. The main part of the efficiency loss in PbGl is due to the effect of bad module and edge cuts which is approximately 40% at high $p_T$ for the PbGl and 20% for the PbSc, respectively.

| $p_T$ | PbGl | | PbSc | |
|---|---|---|---|---|
| | 3.25 GeV/$c$ | 8.5 GeV/$c$ | 3.25 GeV/$c$ | 8.5 GeV/$c$ |
| $a_{\Delta y}$ | 0.068 | 0.080 | 0.216 | 0.246 |
| $\varepsilon$ | 0.351 | 0.358 | 0.455 | 0.515 |
| $c_{\text{conv}}$ | 0.93 | 0.93 | 0.90 | 0.90 |
| $c_{\gamma\gamma}$ | 0.98798 | | | |

points in Fig. 5 (lower), which show the ratio of the yield from the two Level-2 trigger samples per *equivalent* number of minimum bias events to the same from the true minimum bias sample itself. We combine the yields obtained in the minimum bias event sample and the LVL2A (LVL2B) trigger sample above a cutoff of 6.5 GeV/$c$ (3.5 GeV/$c$) where the trigger reaches efficiencies greater than 0.4 such that the correction factor is not allowed to be large. A conservative error of 3% is assigned to the efficiency calculations, resulting in a total error of $\sim$3–5%, based on the three studies: (1) comparisons of the data shown in Fig. 5, (2) comparisons of the two calculational methods, and (3) a study of the yields in the subsample of minimum bias events that also fired the triggers, similar to (1).

### 3. Other corrections

The calculated corrections are applied to the raw $\pi^0$ yield as given by Eq. (5). Table II shows the corrections in central collisions for two different bins in transverse momentum and for the PbGl and PbSc, respectively. As discussed above the effect of the cut on bad modules is included in the efficiency correction, due to its dependence on the depth of the electromagnetic shower.

Following the usual PHENIX procedure of modifying the quoted yield values for each finite sized $p_T$ bin such that the measurement corresponds to $p_T$ value at the bin center instead of the average $p_T$ of the bin [49] (thereby facilitating taking ratios of spectra from different collision systems), a final correction is applied to the *yield* of each data point. Using a continuous function that is fit to the data points, values for the invariant yields at the centers of the chosen $p_T$ bins are scaled by the ratio of the fit value at the fit's average $p_T$ to the fit value at the bin center. This is an iterative procedure similar to the final efficiency correction described in Sec. III D1 above, with a smaller convergence criteria of <0.1% of the previous correction. The fit function is empirically determined and several functional forms were found to give similar performance (e.g., see Fig. 6 below) and negligible differences in the resulting corrections. All the functional forms either explicitly contain or implicitly converge quickly to, a pure power law form (const/$p_T^n$) above $p_T \sim 4$ GeV/$c$.
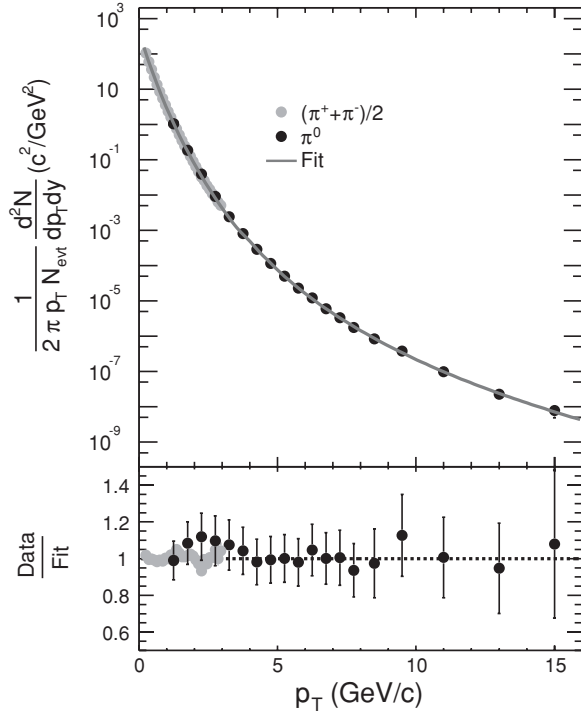
FIG. 6. Comparison of the combined $\pi^0$ result to the measurement of charged pions within the PHENIX experiment in minimum bias events. The fit (see previous Sec. III D 3) considers the averaged result of the $\pi^+$ and $\pi^-$ measurement [7] below $p_T = 3\,\mathrm{GeV}/c$ and the $\pi^0$ data above.

The spectral shape is discussed further under Secs. IV A and IV B.

#### 4. Systematic errors

Each correction of the raw yield following Eq. (5) is afflicted with its own uncertainty, but already the determination
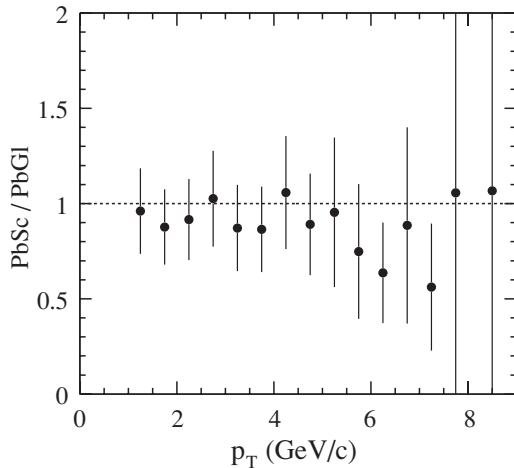


FIG. 7. Comparison of fully corrected spectra for the PbGl and the PbSc for peripheral events. Similar consistency is observed for all centralities. The error bars represent the statistical and systematic uncertainties.

of the $\pi^0$ raw yield itself is sensitive to the method of extraction. In particular it is sensitive to the choice of the fit function for the background scaling and the extraction window. In principle, both should be taken into account by the detector efficiency, but in the efficiency calculation no background subtraction is necessary. For this reason the systematic error of the peak extraction method is determined in two steps: first via the comparison of the raw yield obtained with two different fits for the background scaling, and second through the comparison of the fully corrected spectra for different sizes of the extraction window, for the real data as well as for the efficiency calculation.

The systematic error introduced by the efficiency calculation is estimated by comparing the fully corrected spectra for different PID criteria as well as for different additional smearing. The smearing (or energy resolution in the simulation) is changed in a way that a clear disagreement between the measured $\pi^0$ peak width and the peak width from the embedding is observed.

Apart from the uncertainty of the efficiency, the main contribution to the systematic error is the determination of the absolute energy scale. Based on the comparison of the $\pi^0$ peak positions in the data to the expectation from simulation the energy scale can only be determined or confirmed with limited accuracy, $\Delta(E)/E = 1.6\%$ in the PbSc and, because of the smaller acceptance, $\Delta(E)/E = 2\%$ in the PbGl.

The additional contributions to the systematic error that have not been discussed in detail involve the uncertainty of the conversion correction (2.9%) and of the acceptance calculation (2.5%) both due to small uncertainties in detector material and alignment. Table III provides a final overview of the various contributions to the total error of the $\pi^0$ measurement in the PbSc and the PbGl, respectively.

The most important cross-check of the final result is the comparison of the result for the two different detector types PbGl and PbSc, which is shown for peripheral events in Fig. 7. A good agreement within the errors is seen and similar consistency is found in all centralities. Because they represent essentially independent measurements, the two

TABLE III. Summary of the dominant sources of systematic errors on the $\pi^0$ yields extracted independently with the PbGl and PbSc electromagnetic calorimeters in central events for different $p_T$. For comparison the statistical uncertainty is also shown.

| $p_T$ (GeV/$c$) | PbGl | | PbSc | |
|---|---|---|---|---|
| | 3.25 | 8.5 | 3.25 | 8.5 |
| Yield extraction | 8.7% | 6.% | 9.8% | 7.3% |
| Efficiency | 11.4% | 11.4% | 11.4% | 11.4% |
| Acceptance | 2.5% | 2.5% | 2.5% | 2.5% |
| Conversions | 2.9% | 2.9% | 2.9% | 2.9% |
| Level-2 data | — | — | — | 3% |
| Energy scale | 13.8% | 14.1% | 10.5% | 11.2% |
| Total syst. | 20.5% | 19.3% | 18.8% | 18.7% |
| Statistical | 10.6% | 50% | 8.1% | 26.6% |

results are averaged and the total error of the combined result is reduced using a standard weighted least-squares method also described in Ref. [50]. An additional cross-check of the final result based on isospin symmetry is provided by the measurement of charged pions in the central arm [7], this is shown for minimum-bias collisions in Fig. 6. The neutral pion measurement smoothly extends the result for charged pions to larger transverse momenta.

### E.  $R_{\mathrm{AA}}(p_T)$ measurement

Using the invariant yields obtained from the above-described analysis and the separately measured invariant cross section for $\pi^0$ production in $p+p$ collisions [46], we calculate the nuclear modification factor, $R_{\mathrm{AA}}$, according to

$$R_{\mathrm{AA}}(p_T) = \frac{\left(1/N_{\mathrm{AA}}^{\mathrm{evt}}\right) d^2 N_{\mathrm{AA}}^{\pi^0}/dp_T\, dy}{\langle T_{\mathrm{AA}}\rangle \times d^2\sigma_{pp}^{\pi^0}/dp_T\, dy}, \qquad (6)$$

where $\langle T_{\mathrm{AA}}\rangle$ is the average Glauber nuclear overlap function for the centrality bin under consideration

$$\langle T_{\mathrm{AA}}\rangle \equiv \frac{\int T_{\mathrm{AA}}(\mathbf{b})\, d\mathbf{b}}{\int \left(1 - e^{-\sigma_{pp}^{\mathrm{inel}} T_{\mathrm{AA}}(\mathbf{b})}\right) d\mathbf{b}}, \qquad (7)$$

from which the corresponding average number of nucleon-nucleon collisions, $\langle N_{\mathrm{coll}}\rangle = \sigma_{pp}^{\mathrm{inel}} \langle T_{\mathrm{AA}}\rangle$, can be easily obtained [51].

### F.  $R_{\mathrm{AA}}(\Delta\phi)$ measurement

The measurement of the raw $\pi^0$ yield with respect to the event reaction plane, $\Delta\phi = \phi(\pi^0) - \Psi$, proceeds as described in Sec. III D for the $p_T$ spectrum except that we measure the yields as a simultaneous function of both $p_T$ and $\Delta\phi$. Because the beam-beam counters have $2\pi$ acceptance, PHENIX can measure the $\pi^0$ yields with uniform acceptance over $0 < \Delta\phi < 2\pi$ even though the electromagnetic calorimeters have only $1\pi$ nominal azimuthal acceptance. Because the measurement of $\Psi$ is ambiguous with respect to a $180°$ rotation of the reaction plane, and because we expect the $\pi^0$ yields to be symmetric with respect to reflection around $\Delta\phi = 0$, we measure the $\pi^0$ yields in six bins of $|\Delta\phi|$ over the range $0 < |\Delta\phi| < \pi/2$. For each $p_T$ bin we evaluate the ratio,

$$R(\Delta\phi_i, p_T) = \frac{\Delta N(\Delta\phi_i, p_T)}{\sum_{i=1}^{6} \Delta N(\Delta\phi_i, p_T)}, \qquad (8)$$

where $N(\Delta\phi_i, p_T)$ is the measured number of $\pi^0$'s in a given $(\Delta\phi, p_T)$ bin, $\Delta\phi_i$ representing one orientation of $\Delta\phi$. Because the PHENIX central arm acceptance is effectively constant as a function of $\Delta\phi$ and we do not expect any azimuthal dependence of our $\pi^0$ efficiency corrections,

$R(\Delta\phi_i, p_T)$ can be written as:

$$R(\Delta\phi_i, p_T) = R_{\mathrm{AA}}(\Delta\phi_i, p_T)/R_{\mathrm{AA}}(p_T). \qquad (9)$$

Using the measured $R_{\mathrm{AA}}(p_T)$ values we can directly convert the $R(\Delta\phi, p_T)$ to $R_{\mathrm{AA}}(\Delta\phi, p_T)$ without having to apply acceptance and efficiency corrections to the reaction-plane dependent yields. These corrections are already included in the $R_{\mathrm{AA}}(p_T)$ values as described above.

However, before applying this procedure we must first correct the $R(\Delta\phi, p_T)$ values for the finite resolution of the reaction plane measurement. One goal of our measurement is to determine $R_{\mathrm{AA}}(\Delta\phi, p_T)$ without assuming any particular functional dependence on $\Delta\phi$. For purposes of correcting for reaction plane resolution, we take advantage of the fact that the observed $\pi^0$ yields and hence the nuclear modification vary with $\Delta\phi$ to first order as

$$R^{\mathrm{raw}}(\Delta\phi, p_T) \approx R_0\big[1 + 2v_2^{\mathrm{raw}}\cos{(2\Delta\phi)}\big], \qquad (10)$$

ignoring the much smaller higher-order harmonics such as $v_4$ terms. The superscript "raw" denotes the values not corrected for the reaction plane resolution. This resolution reduces $v_2$ by the factor $\sqrt{2\langle\cos 2(\Psi_1 - \Psi_2)\rangle}$ [44], which is given by the independent measurement of $\Psi$ in the two BBC's shown previously in Fig 1. For each $p_T$ bin in a given centrality class we fit the $R(\Delta\phi, p_T)$ values to the functional form in Eq. (10) and then correct each measured $R(\Delta\phi, p_T)$ value according to

$$R^{\mathrm{corr}}(\Delta\phi, p_T) = R^{\mathrm{raw}}(\Delta\phi, p_T)\left[\frac{1 + v_2^{\mathrm{corr}}\cos{(2\Delta\phi)}}{1 + v_2^{\mathrm{raw}}\cos{(2\Delta\phi)}}\right], \quad (11)$$

with $v_2^{\mathrm{corr}} = v_2^{\mathrm{raw}}/\sqrt{2\langle\cos 2(\Psi_1 - \Psi_2)\rangle}$. We estimate the systematic error in the reaction plane resolution correction by propagating the centrality dependent uncertainties in $\sqrt{2\langle\cos 2(\Psi_1 - \Psi_2)\rangle} = \langle\cos 2(\Psi_{\mathrm{meas}} - \Psi_{\mathrm{true}})\rangle$ from Table I. Of course, the above-described correction only strictly applies if $R_{\mathrm{AA}}(\Delta\phi)$ is well described by the functional form in Eq. (10). Although we do observe some departure from this harmonic form in the data, the differences are typically below 5% so our correction will not introduce a large error.

## IV. RESULTS

### A.  $\pi^0$ transverse-momentum spectra and nuclear modification factors

The $\pi^0$ invariant yields obtained using the procedure described in Sec. III D are presented in Fig. 8 as a function of $p_T$ for the nine chosen centrality bins. With the increased statistics included in this analysis, we have extended the $p_T$ range of the previous PHENIX measurement by at least 2 GeV/$c$ for all centrality bins. The $p_T$ range of the central bin has been extended from 10 to 14 GeV/$c$. Where the spectra overlap, the results shown here are consistent with the previously published results within systematic errors. The errors shown on the points in Fig. 8 include statistical errors and point-to-point varying systematic errors. The appendix tabulates the $\pi^0$ spectra plotted in Fig. 8 (centralities: 0–10, 10–20, . . . , 70–80, 80–92%) plus the combined spectra for centralities 0–20, 20–60, and 60–92%, which are used for

comparison to other neutral meson measurements [13]. The spectra in Fig. 8 depart from the exponential-like shape above 3 GeV/$c$, which is consistent with the expectation that high-$p_T$ hadron production is dominated by hard-scattering processes that produce a power-law $p_T$ spectrum [52] for hadrons resulting from quark and gluon fragmentation.

In previous publications, we have established the suppression of high-$p_T$ $\pi^0$ production in Au+Au collisions [3,6]. This suppression cannot be easily seen given the large range of invariant yield covered by Fig. 8.

To evaluate the suppression of high-$p_T$ $\pi^0$'s, we show in Fig. 9 the $p_T$ dependence of the $\pi^0$ nuclear modification factor, $R_{AA}(p_T)$, for the nine individual bins of collision centrality and for the full minimum-bias centrality range 0–92.2%. We make use of the PHENIX Run3 $p+p$ baseline $\pi^0$ data. [47]. The error bars on the data in Fig. 9 include contributions from statistical errors in the Au+Au and $p+p$ measurements and from the systematic errors that do not cancel between the measurements. The separate band shown in each panel indicates $p_T$-independent errors on the $R_{AA}$ measurement

resulting from uncertainties in estimating $T_{AA}(x, y)$ and systematic errors on the normalization of the Au+Au and $p+p$ measurements that do not cancel. As in previously published articles (e.g., Refs. [4,5,7]), a factor of ∼5 high $p_T$ $\pi^0$ suppression in the most central Au+Au collisions, $R_{AA} \approx 0.2$, is observed, with the suppression approximately $p_T$ independent for $p_T > 5$ GeV/$c$. The suppression at high $p_T$ decreases in more peripheral collisions such that the two most peripheral bins have $R_{AA}$ values consistent with unity for $p_T > 3$ GeV/$c$.

### B. Suppression via spectrum shift

The suppression of high-$p_T$ particles as shown above was determined by comparison of the semi-inclusive measured yields as a function of centrality in Au+Au collisions at $\sqrt{s_{NN}} = 200$ GeV to the $\langle T_{AA} \rangle$ scaled $p_T$ spectrum from $p+p$ collisions [53]. A direct comparison of the 0–10% centrality Au+Au spectrum to the scaled $p+p$ spectrum is shown in Fig. 10 as a log-log plot to emphasize the pure power law
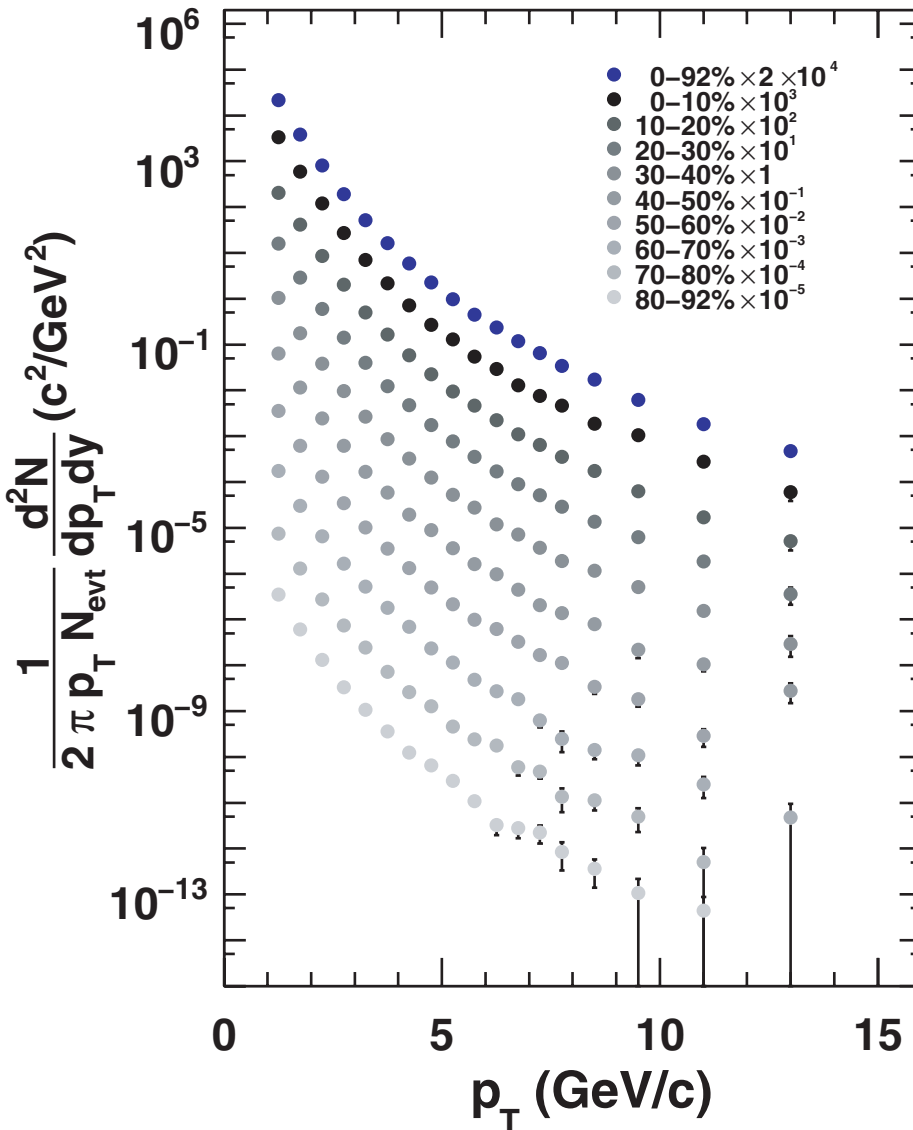


FIG. 8. (Color online) Neutral pion invariant yields as a function of $p_T$ measured in minimum bias and nine centrality classes in Au+Au collisions at $\sqrt{s_{NN}} = 200$ GeV. Spectra for different centralities are scaled for clarity. Errors are total errors, full systematic, and statistical added in quadrature.
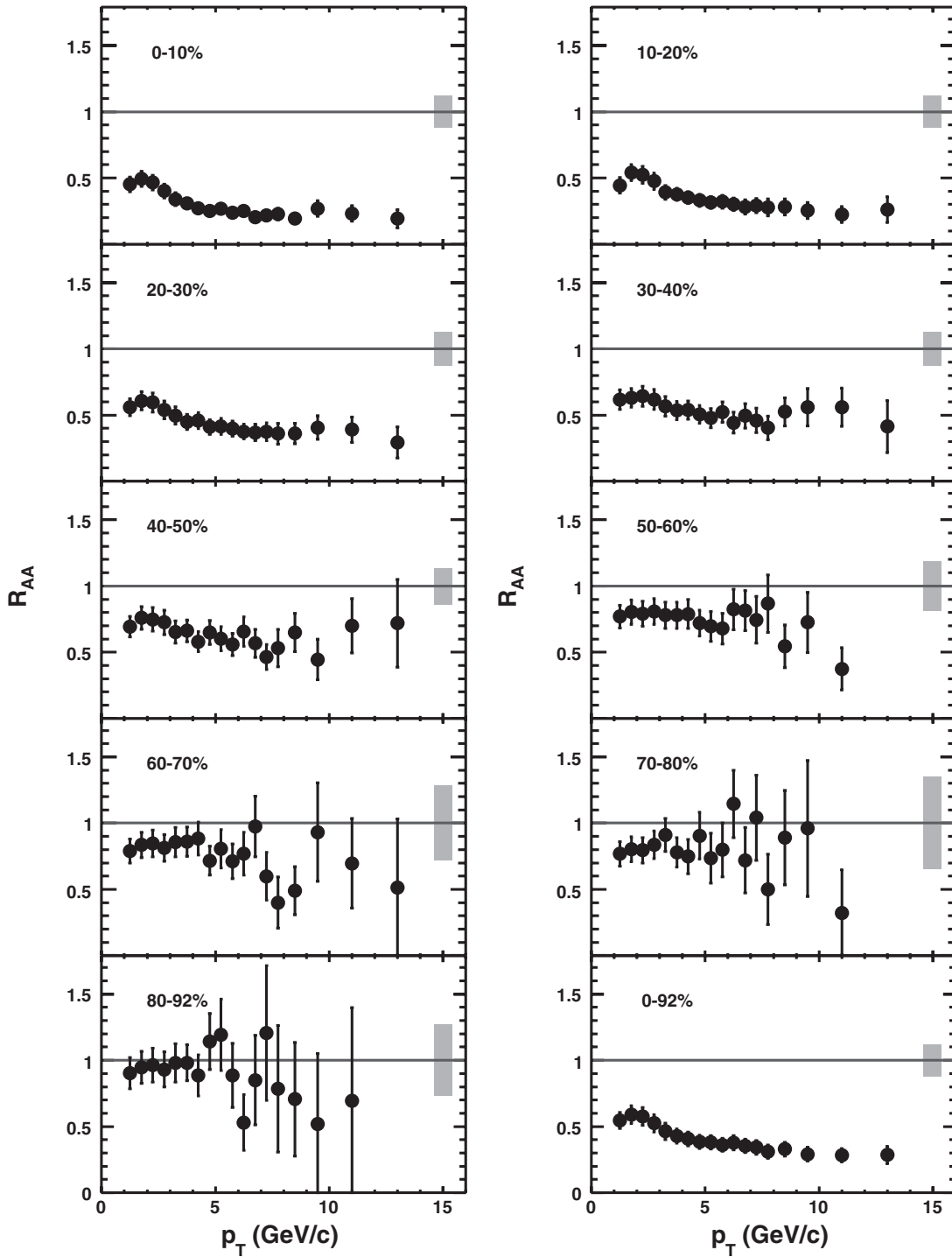
FIG. 9. Nuclear modification factor $R_{AA}$ for neutral pions as a function of $p_T$ for different centralities. The shaded error band around unity indicates the uncertainty in scaling factor $T_{AA}$ and an overall scale uncertainty in the $p+p$ reference.

dependence of the data for $p_T > 3$ GeV/$c$. The suppression is commonly expressed by taking $R_{AA}$ the ratio of the point-like scaled semi-inclusive yield to the reference distribution [Eq. (6)].

As illustrated in Fig. 10, instead of viewing the suppression in the nuclear modification factor as "vertical" reduction of the Au + Au yields, it can equally well be taken as a "horizontal"

shift in the $\langle T_{AA}\rangle$ scaled Au+Au spectrum, such that

$$\frac{(1/N_{AA}^{evt})d^2N_{AA}(p_T)/dp_Tdy}{\langle T_{AA}\rangle} = \frac{d^2\sigma_{pp}[p_T'=p_T+S(p_T)]}{dp_T'dy}$$
$$\times [1+dS(p_T)/dp_T], \quad (12)$$

where the last term in parenthesis is the Jacobian, $dp_T'/dp_T$.
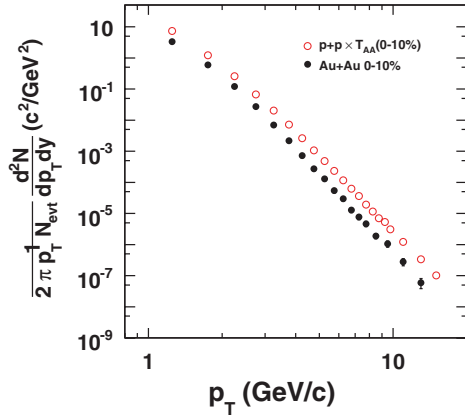
FIG. 10. (Color online) Log-log plot of central Au+Au and scaled $p+p$ $\pi^0$ $p_T$ distributions.

Furthermore, owing to the pure power law of the $p+p$ reference spectrum, $Ed^3\sigma/dp^3 \propto p_T^{-n}$ with $n = 8.10 \pm 0.05$ above $p_T \approx 4$ GeV/$c$, the relative shift of the spectra—assumed to be the result of energy loss for the Au+Au spectrum—is easily related to the equivalent ratio, $R_{AA}(p_T)$:

$$R_{AA}(p_T) = \frac{[p_T + S(p_T)]^{-n+1}}{p_T^{-n+1}}[1 + dS(p_T)/dp_T] \quad (13)$$

$$= [1 + S(p_T)/p_T]^{-n+1}[1 + dS(p_T)/dp_T]$$

where the exponent is $n - 1$ because the relevant shift is in the $d\sigma/dp_T$ spectrum rather than in $d\sigma/p_T\,dp_T$. The fact that the Au+Au and reference $p+p$ $p_T$ spectra are parallel in Fig. 10 provides a graphical illustration that the fractional $p_T$ shift in the spectrum, $S(p_T)/pt = S_0$, is a constant for all $p_T > 3$ GeV/$c$, which also results in a constant ratio of the spectra, $R_{AA}(p_T)$. For the constant fractional shift, the Jacobian is simply $dS(p_T)/dp_T = S_0$ and Eq. (13) becomes:

$$R_{AA}(p_T) = (1 + S_0)^{-n+2}, \quad (14)$$

$$R_{AA}(p_T)^{1/(n-2)} = \frac{1}{1 + S_0}. \quad (15)$$

The effective fractional energy loss, $S_{\rm loss}$, is related to the fractional shift in the measured spectrum, $S_0$. The hadrons that would have been produced in the reference $p+p$ spectrum at transverse momentum $p_T + S(p_T) = (1 + S_0)p_T$, were detected with transverse momentum, $p_T$, implying a fractional energy loss:

$$S_{\rm loss} = 1 - 1/(1 + S_0) = 1 - R_{AA}(p_T)^{1/(n-2)}. \quad (16)$$

The fractional energy loss $S_{\rm loss}$ as a function of centrality expressed as $N_{\rm part}$ is shown in Fig. 11 for two different $p_T$ ranges, $3 < p_T < 5$ GeV/$c$ and $5 < p_T < 7$ GeV/$c$. There appears to be a small decrease of $S_{\rm loss}$ with increasing $p_T$, but the main observation from Fig. 11 is that $S_{\rm loss}$ increases approximately like $N_{\rm part}^{2/3}$, as suggested by GLV [54] and PQM [55].
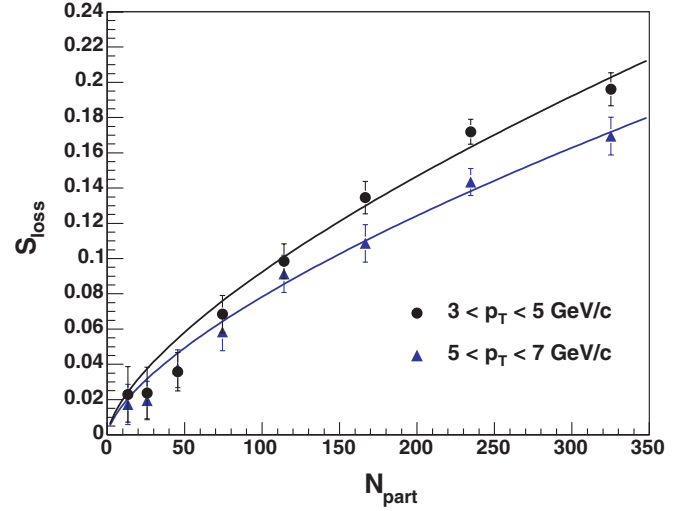


FIG. 11. (Color online) Fractional energy loss $S_{\rm loss}$ obtained from Eq. (16) versus centrality given by $N_{\rm part}$. The lines are fits of the form $\propto N_{\rm part}^{2/3}$ for each $p_T$ range.

It is important to realize that the effective fractional energy loss, $S_{\rm loss}$ estimated from the shift in the $p_T$ spectrum, is actually less than the real average energy loss at a given $p_T$, i.e., the observed particles have $p_T$ closer to the original value than to the average. The effect is similar to that of "trigger bias" [56] where, due to the steeply falling spectrum, the $\langle z \rangle$ of detected single inclusive particles is much larger than the $\langle z \rangle$ of jet fragmentation, where $z = \vec{p}_{\pi^0} \cdot \vec{p}_{\rm jet}/p_{\rm jet}^2$. Similarly for a given observed $p_T$, the events at larger $p_T'$ with larger energy loss are lost under the events with smaller $p_T'$ with smaller energy loss.

It should be noted that fluctuations due to the variation of the path length and densities traversed by different partons also contribute to the difference between the true $S_{\rm loss}$ ($S_{\rm loss}^{\rm true}$) and that which is observed ($S_{\rm loss}^{\rm obs}$). However, as long as the dependencies of the induced energy loss on path length and parton energy approximately factorize, these fluctuations will also produce a $p_T$-independent reduction in $S_{\rm loss}^{\rm obs}$ compared to $S_{\rm loss}^{\rm true}$.

### C. Angle dependence of high $p_T$ suppression

To try to separate the effects of the density of the medium and path length traversed, we study the dependence of the $\pi^0$ yield with respect to the reaction plane. For a given centrality, variation of $\Delta\phi$ gives a variation of the path length traversed for fixed initial conditions, whereas varying the centrality allows determination of the effect of varying the initial conditions.

Figures 12 and 13 show the nuclear modification factor $R_{AA}$ as a function of $\Delta\phi$ integrated over $3\,{\rm GeV}/c < p_T < 5\,{\rm GeV}/c$ and $5\,{\rm GeV}/c < p_T < 8\,{\rm GeV}/c$, respectively. For all centralities (eccentricities) considered, there is almost a factor of 2 more suppression out-of-plane ($\Delta\phi = \pi/2$) than in-plane ($\Delta\phi = 0$), something that is immediately apparent in viewing the data in this fashion—explicitly displaying information that is implicit only in $R_{AA}$, $v_2$, or the combination thereof.
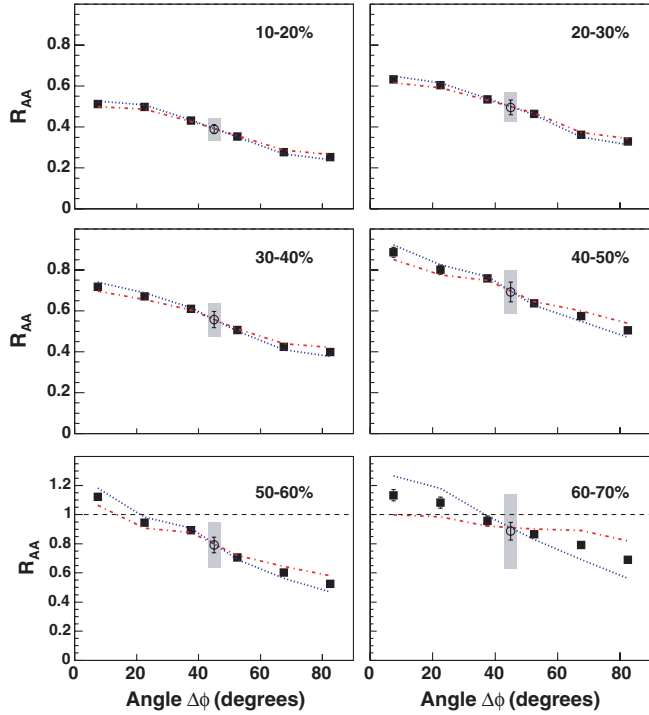
FIG. 12. (Color online) $R_{AA}$ versus $\Delta\phi$ for $\pi^0$ yields integrated over $3 < p_T < 5$ GeV/$c$. Most statistical errors are smaller than the size of the points. The lines following the data points show the bin-to-bin errors resulting from the uncertainty in the reaction plane resolution correction (Fig. 1) and from bin-to-bin uncertainties in the $R_{AA}$ values. The shaded band indicates the overall $R_{AA}$ uncertainty.

Strikingly, in contradiction to the data the variation in $R_{AA}$ with respect to the reaction plane expected by parton energy loss models [29,57] should be much smaller for the more peripheral bins than for the central bins. As a result, the suppression vanishes (and perhaps an enhancement is observed) for smaller $\Delta\phi$ in the peripheral bins, corresponding to small path length traversed in the medium. Although collective elliptic flow effects, usually not included in those models, are known to boost in-plane (compared to out-of-plane) particle production [2,42], it is unclear how such collective effects can still play such an important role at the high-$p_T$ bins considered. This may point to the possible need for a formation time before suppression can occur [58] and which could also explain why attempts to describe the azimuthal asymmetry $v_2$ solely in terms of purely geometrical energy loss have failed. Figures 14 and 15 give the angular dependence in terms of the fractional energy loss $S_{loss}$, and provide essentially the same information as shown in the plots of $R_{AA}(\Delta\phi)$ in Figs. 12 and 13. Once again we see a large variation in energy loss as a function of angle. All the measurements of $R_{AA}$ or equivalently $S_{loss}$ vs. reaction plane and centrality, provide new constraints to models of jet quenching. To better understand the implications of the results shown in these figures, we will attempt in the next section to find a common geometric description of the angle and centrality dependences in terms of an estimated path length of the parton in the medium.
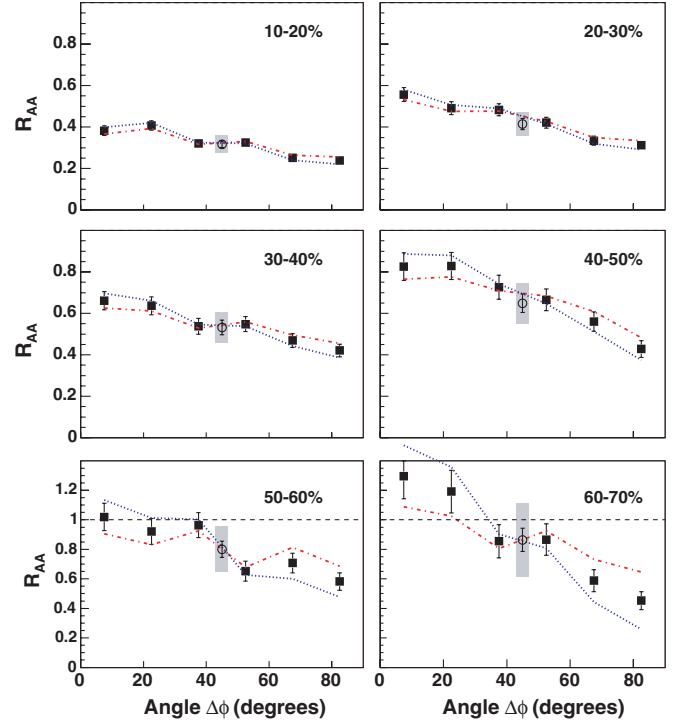


FIG. 13. (Color online) $R_{AA}$ versus $\Delta\phi$ for $\pi^0$ yields integrated over $5 < p_T < 8$ GeV/$c$. The error lines and band are the same as in Fig. 12.
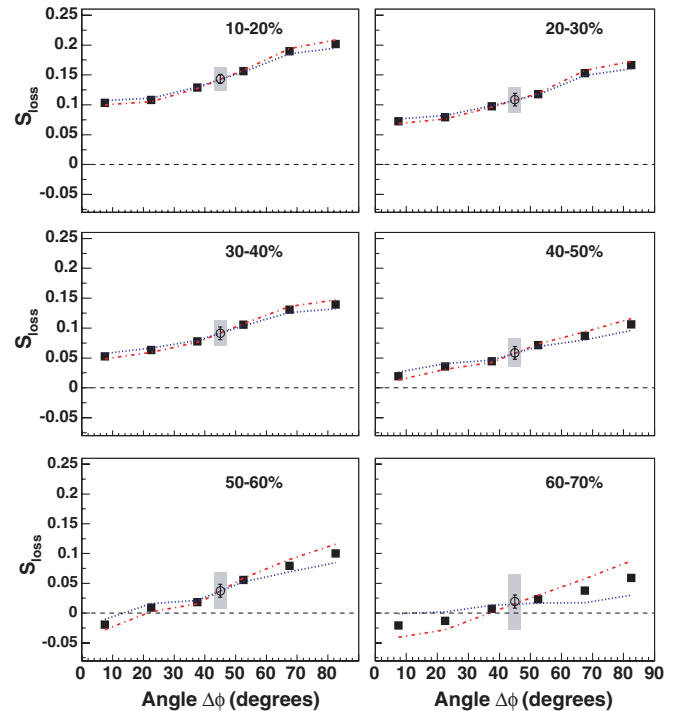


FIG. 14. (Color online) $S_{loss}$ versus $\Delta\phi$ for $\pi^0$ yields integrated over $3 < p_T < 5$ GeV/$c$. The statistical errors are smaller than the size of the points. The lines following the data points show the bin-to-bin errors resulting from the uncertainty in the reaction plane resolution correction (Fig. 1) and from bin-to-bin uncertainties in the $S_{loss}$ values. The shaded band indicates the overall $S_{loss}$ uncertainty.
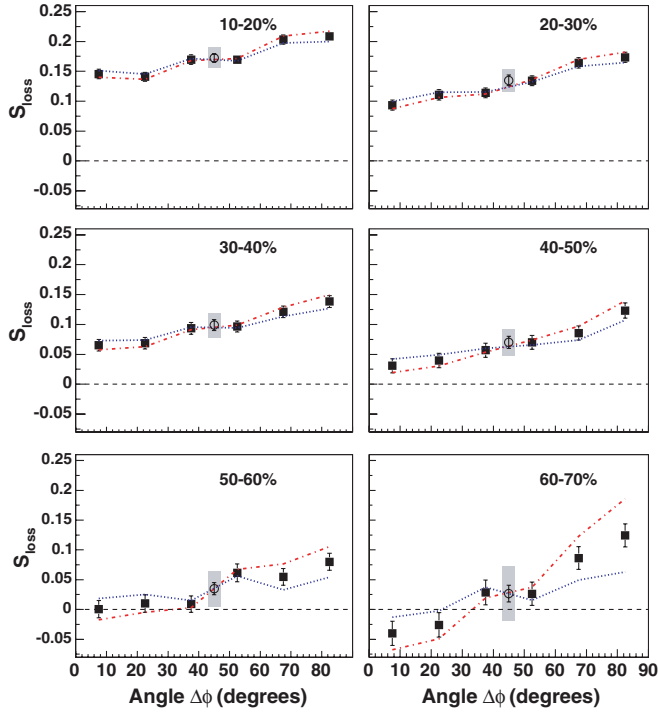
FIG. 15. (Color online) $S_{loss}$ versus $\Delta\phi$ for $\pi^0$ yields integrated over $5 < p_T < 8$ GeV/$c$. The error lines and band are the same as in Fig. 14.

### D. Path-length dependence of energy loss

To analyze the path-length dependence of parton energy loss using the data presented here we will use different methods for estimating the path lengths of partons in the medium as a function of centrality and $\Delta\phi$. The "standard" approach would be to evaluate a length-weighted integral of the participant charge density in the medium along the parton path. We will adopt such an approach, described by the parameter $L_{xy}$ defined below, but we will also consider two other simplified approaches that may help indicate which physics is most relevant in determining the observed suppression. We first consider, simply, $L_\varepsilon$, the distance from the edge to the center of the elliptical overlap zone of the Au+Au collision to represent the average path length of a parton in the medium. Then we try to weight the path length (or length-squared) traversed by a parton from the center of the ellipse by the participant density in the transverse plane: $\rho L(\Delta\phi)$ [$\rho L^2(\Delta\phi)$]. Finally, we do the same path-length weighting for partons produced across the overlap ellipse, with hard-scattering production points weighted by $T_{AA}(x, y)$: $\rho L_{xy}$ ($\rho L_{xy}^2$). It is obvious that such a $\Delta\phi$-dependent analysis is not possible from just a simple combination of $R_{AA}$ and $v_2$.

In detail, the three approaches considered here are as follows:

(i) The simplest picture for the angular dependence of the energy loss in noncentral collisions is that it is due to the asymmetric shape of the overlap region of the colliding nuclei. Taking this idea to its extreme, only

the simplest length scale, the length of the overlap region in a particular direction, matters.

To evaluate this length, we first estimated the root-mean-square radius and eccentricity of an ellipse approximating the shape of the overlap region from the transverse distribution of the participant density calculated using standard Glauber Monte Carlo techniques in which all variations of impact parameter, etc., for a given centrality class are taken account in the quoted errors of the geometrical quanties [51]. Only the errors on the averages are considered; for instance, the fluctuations in the event-by-event participant eccentricity are taken into account in the quoted error of the centrality averaged $\varepsilon$. We then estimated the path length, $L_\varepsilon$, of partons emitted at a given angle $\Delta\phi$ by evaluating the distance from the center of ellipse to the edge. For each centrality, the value of $L_\varepsilon$ is calculated as a function of $\Delta\phi$:

$$L_\varepsilon = \frac{b\sqrt{1+\varepsilon}}{\sqrt{1+\varepsilon\cos(2\Delta\phi)}}, \tag{17}$$

where $b = \sqrt{\langle x^2 \rangle}$, the root-mean-square semiminor axis (conventionally taken in the $x$ direction) and $\varepsilon = (\langle y^2 \rangle - \langle x^2 \rangle)/(\langle y^2 \rangle + \langle x^2 \rangle)$ are taken from the Monte Carlo Glauber calculation. The errors on $b$ and $\varepsilon$ are propagated through Eq. (17) for the error on $L_\varepsilon$. A plot of $L_\varepsilon$ as a function of centrality and $\Delta\phi$ is shown in Fig. 16.

As described previously in Section III F, the effect and associated uncertainties of reaction plane resolution are
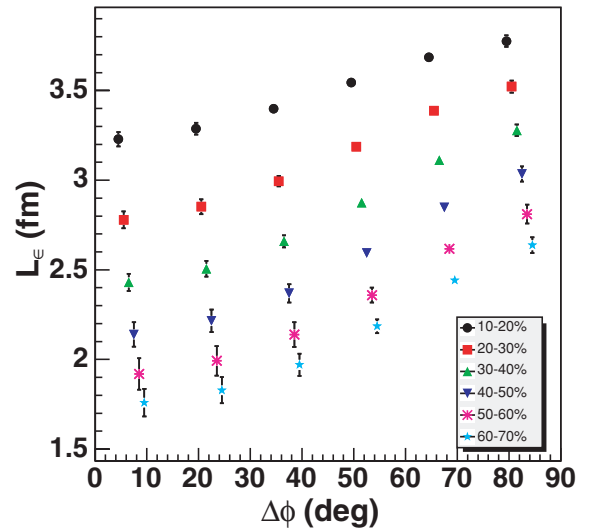


FIG. 16. (Color online) Simple geometrical length estimator $L_\varepsilon$ with uncertainties plotted *vs.* angle with respect to reaction plane, plotted for the six centralities considered as indicated in the legend. The angle with respect to reaction plane, $\Delta\phi$, is for the center of the bins ($7.5°$, $22.5°$, $37.5°$, $52.5°$, $67.5°$, and $82.5°$), the same for all centralities. For visual clarity a centrality dependent offset is introduced.

taken into account (i.e., corrected for) in the values and quoted errors of $R_{AA}(\Delta\phi)$. Thus detector effects of reaction plane resolution should not be considered in the evaluation of $L_\varepsilon$.

(ii) Although the participant density is used to evaluate the dimensions of the ellipse, the above analysis ignores the dependence of participant density on position in the transverse plane. Thus as a natural extension of the simple length scale in (i), for another analysis of the dependence of energy loss on $\Delta\phi$, we assume that the color-charge density in the medium is proportional to participant density (see Refs. [29,59]) and evaluate $\rho L$, the integral of this density along the path length of the particle. This quantity is proportional to the opacity of the medium ($n = L/\lambda$) divided by some undetermined

cross section. Although the integral in principle extends to infinity the participant density naturally cuts off the integral outside the collision zone.

$$\rho L = \int_0^\infty dr \, \rho_{\text{part}}(r, \Delta\phi). \qquad (18)$$

To account for the possible role of LPM coherence in the energy loss process, we evaluate a similar quantity, including an extra factor of $r$ in the integrand.

$$\rho L^2 = \int_0^\infty dr \, r\rho_{\text{part}}(r, \Delta\phi). \qquad (19)$$

We note that a Bjorken $1/\tau$ expansion of the medium would approximately cancel one power of $r$ in the above expressions. Then, $\rho L$, might represent LPM energy
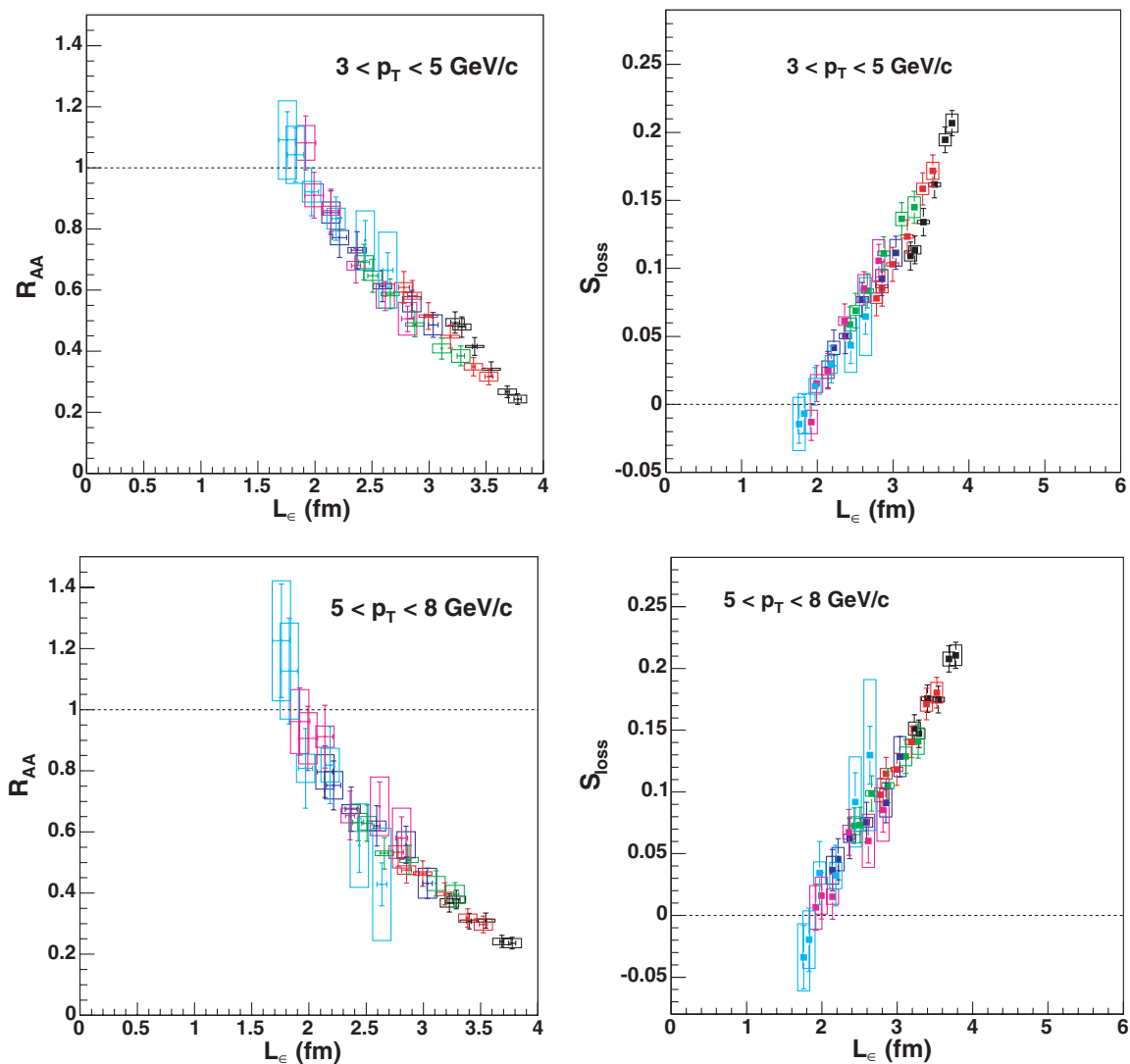


FIG. 17. (Color online) $R_{AA}$ and $S_{\text{loss}}$ versus $L_\varepsilon$ whose definition is explained in the text. Each data point represents a centrality bin and $\Delta\phi$ (azimuth defined *w.r.t.* the reaction plane) bin combination. The six centrality bins are denoted by different colors as follows: cyan, 60–70%; mauve, 50–60%; blue, 40–50%; green, 30–40%; red, 20–30%; black, 0–10%. Within each centrality group, the six different data points correspond to the same $\Delta\phi$ bins as in Figs. 12–15. The height of the bars around each data point represent the systematic error in $R_{AA}(\Delta\phi)$ ($S_{\text{loss}}$) corresponding to $L_\varepsilon$.
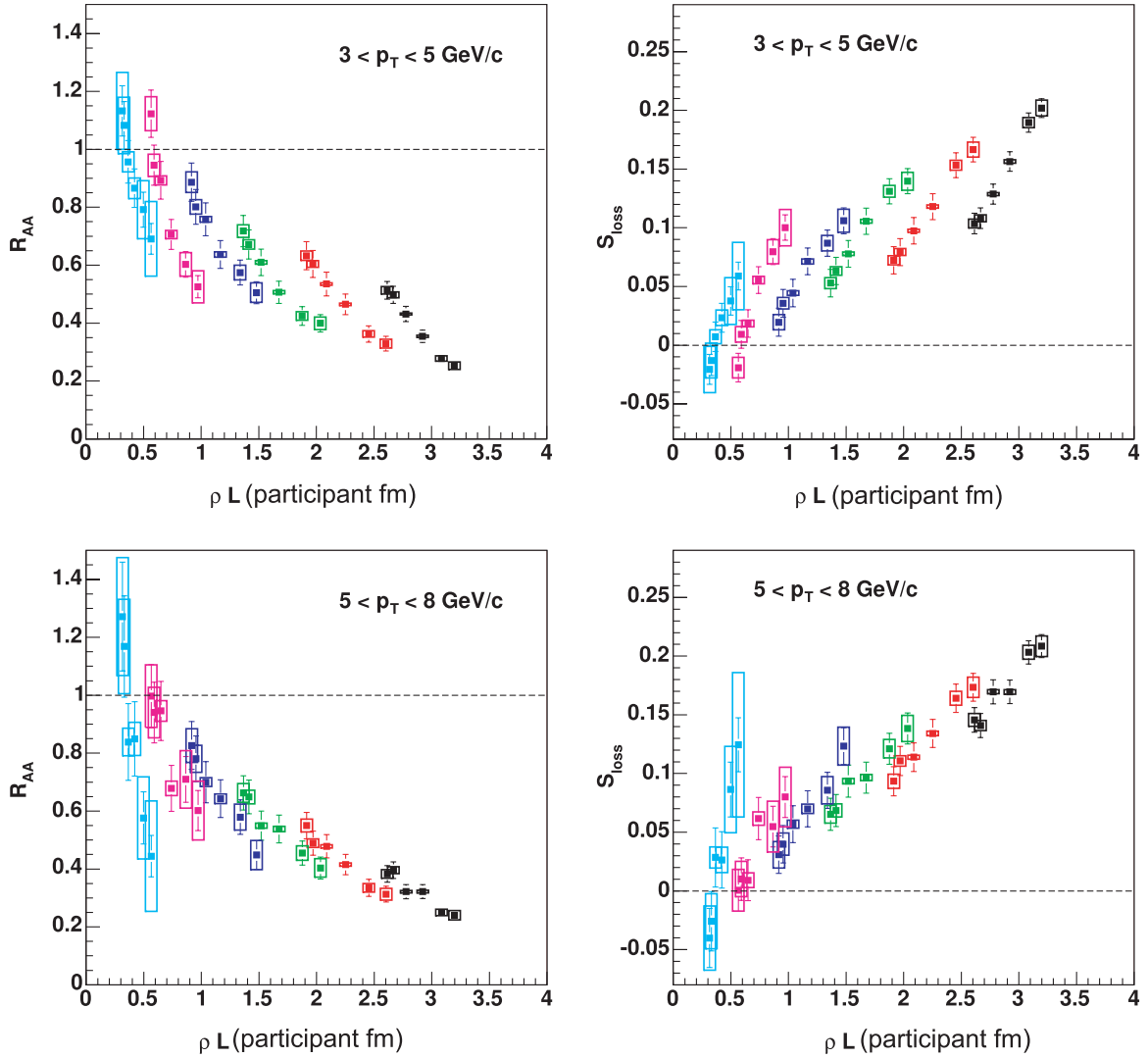
FIG. 18. (Color online) $R_{AA}$ and $S_{loss}$ versus $\rho L$, the participant density-weighted path length. The units of $\rho L$ are (nucleon) participants times fm. Colors/data points as in Fig. 17.

loss in the presence of one-dimensional expansion. In the above integrals we assume all jets originate at the center of the collision region similar to our assumption for $L_\varepsilon$.

(iii) A final refinement on our geometrical calculation evaluates integrals like those in Eq. (18) for jet production points distributed over the collision region to better account for geometric fluctuations. We are using a Monte Carlo algorithm to sample jet production points $(x_0, y_0)$ according to $T_{AA}(x, y)$ weighting and $\Delta\phi$ angles from a uniform distribution. For each jet, we evaluate the integral of the color-charge density (assumed $\propto$ participant density as above) along the path of the parton out of the medium,

$$\rho L_{xy} = \int_0^\infty dl \, \rho_{part}(x_0 + l\cos\Delta\phi, y_0 + l\sin\Delta\phi). \tag{20}$$

The above Monte Carlo sampling yields a distribution of $\rho L_{xy}$ values for each centrality. The larger values of $\rho L_{xy}$ correspond to larger energy loss, which means these jets will have smaller contribution to the observed yield. To take this into account, a weighting factor is applied when evaluating $\langle \rho L_{xy} \rangle$. We assume that the energy loss can be represented by our empirical energy loss, $S_{loss}$ which we take to be proportional to $\rho L_{xy}$ but with an undetermined multiplicative constant, $\kappa$. We determine this constant in each centrality bin by relating $S_{loss}$ to $R_{AA}$ using Eq. (16) and then evaluating the survival probability of each jet through

$$P_{surv}(\rho L_{xy}) = 1 - (\kappa \rho L_{xy})^{(n-2)} \tag{21}$$

and requiring that the resulting suppression summed over all sampled jets agrees with the measured $\Delta\phi$-integrated $R_{AA}$ for that centrality bin. This determines the constant $\kappa(N_{part})$ and allows us to
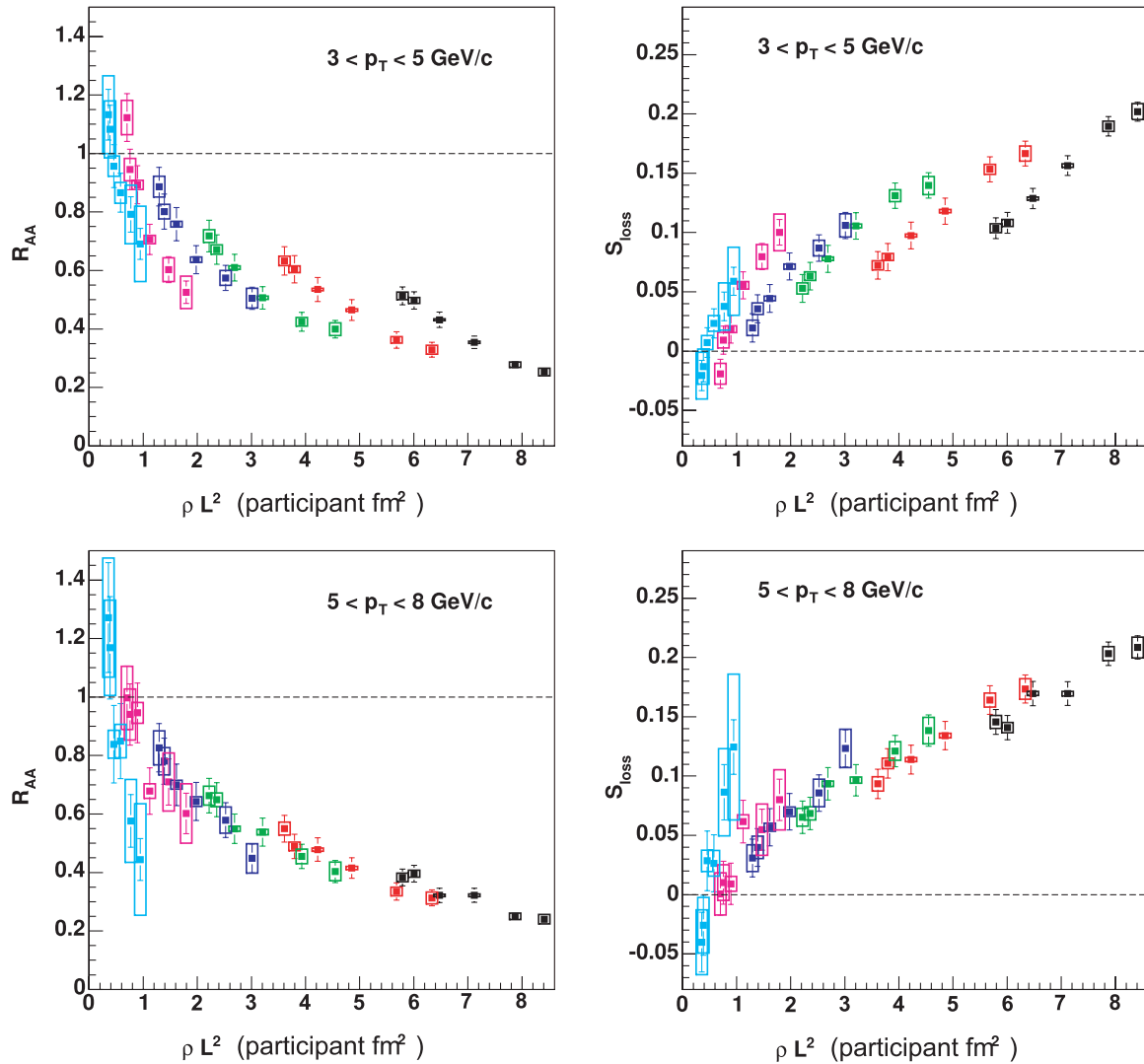
FIG. 19. (Color online) $R_{AA}$ and $S_{loss}$ versus $\rho L^2$, the density-weighted path length squared. The units of $\rho L^2$ are (nucleon) participants times fm squared. Colors/data points as in Fig. 17.

evaluate a survival probability weighted average for $\rho L_{xy}$.

We now evaluate how well the three above-described treatments of the geometry of the parton propagation in the medium perform in providing a consistent description of the $\Delta\phi$ *and* centrality dependence of $\pi^0$ suppression.

The plots shown in Figs. 17–21 illustrate the path-length and path-density line-integral dependence of suppression using our empirical estimators. The integral of the $\rho_{part}$ density (i.e., its normalization) is commonly called the "number of participants" $N_{part}$. The systematic error, mostly from $N_{part}$, in the estimators due to the uncertainty of the overlap geometry parameter in a centrality class is approximately 10–20%, decreasing with centrality and is not included in the figures. This uncertainty is derived by propagating the impact parameter and eccentricity uncertainties from the PHENIX Glauber MC itself [1,41].

From Figs. 17–21 it is evident that the individual centrality bins exhibit roughly parallel linear dependencies of the variables vs $\rho L_{xy}$, etc. For the $3 < p_T < 5$ GeV/*c* bin these slopes are such that the curves are disjoint due to the steeper value of the slopes in each centrality group (each color in the plots) compared to the bin-to-bin trend. For the higher $5 < p_T < 8$ GeV/*c* bin, the slopes in the individual centralities flatten such that they follow the bin-to-bin trend much better. These are meant to be qualitative statements. We defer further quantitative tests, e.g., statistical tests, to subsequent data sets (e.g., the larger PHENIX 2004–2005 Run4 data set) with which we can improve statistical precision.

In this spirit, we note several other interesting qualitative dependencies:

(i) $R_{AA}$ is universal as a function of $L_\varepsilon$ for all centrality classes and both $p_T$ ranges.
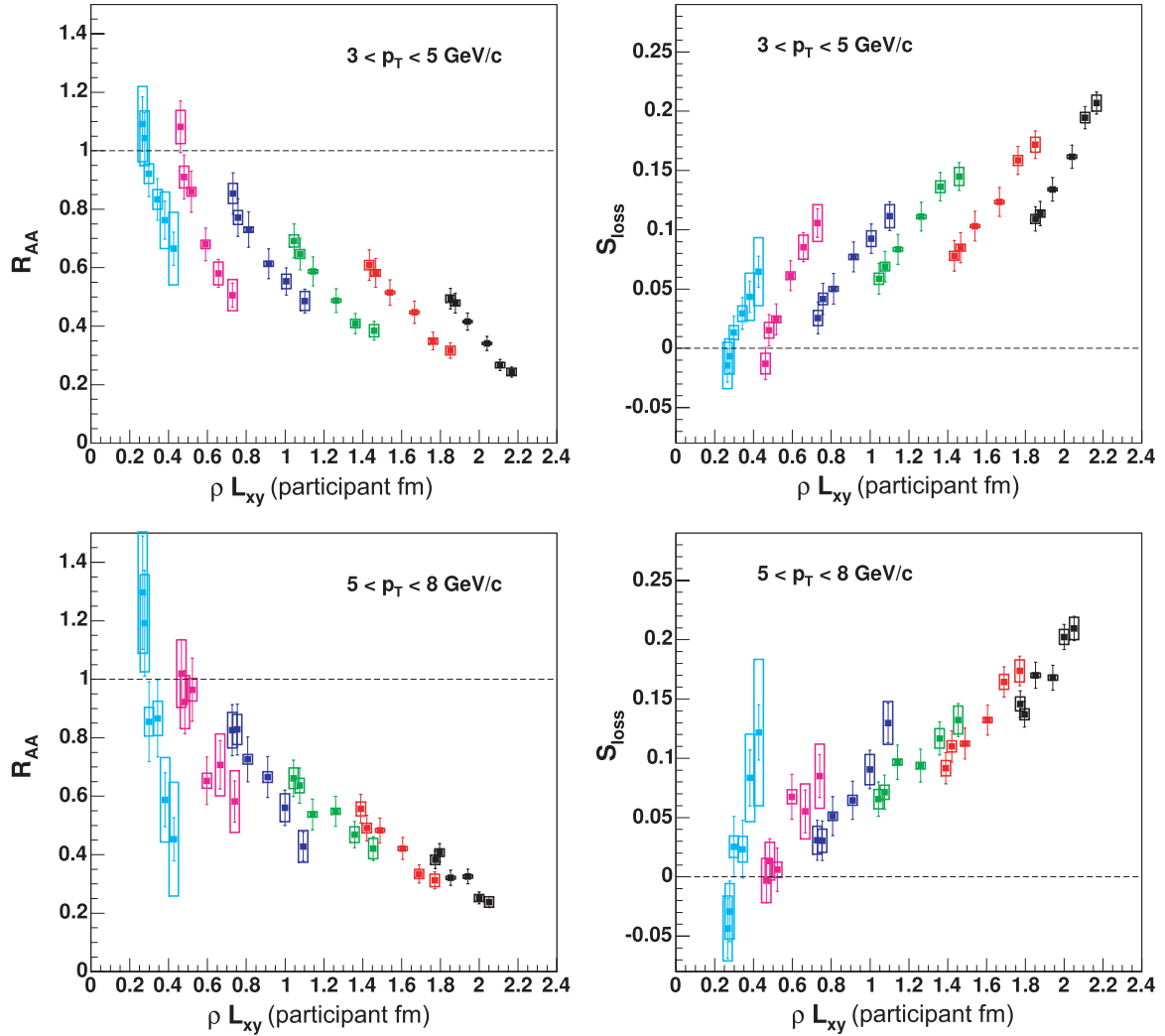
FIG. 20. (Color online) $R_{AA}$ and $S_{loss}$ versus $\rho L_{xy}$ whose definition is explained in the text. The units of $\rho L_{xy}$ are (nucleon) participants times fm. Colors/data points as in Fig. 17.

(ii) $S_{loss}$ is universal and is a linear function of $L_\varepsilon$ for all centrality classes and both $p_T$ ranges.

(iii) Within our errors, we see no suppression $R_{AA} \approx 1$, hence no apparent fractional energy loss $S_{loss}$ for $L_\varepsilon \lesssim 2$ fm.

(iv) Neither $R_{AA}$ nor $S_{loss}$ is universal as a function of $\rho L$, $\rho L^2$, or $\rho L_{xy}$ for $3 < p_T < 5$ GeV/$c$.

(v) For the higher $5 < p_T < 8$ GeV/$c$ $p_T$ bin, $S_{loss}$ ($R_{AA}$) approaches universality as a function of $\rho L^2$, $\rho L$, and $\rho L_{xy}$ (possibly to a lesser extent for the latter two) but does not achieve the level of universality found for $L_\varepsilon$. The largest deviations from universality in these quantities are toward the longer axis (perpendicular to the event plane) in the more peripheral events. The dependence of $S_{loss}$ is reasonably linear as a function of $\rho L$ but tends to level off at larger values of $\rho L^2$.

(vi) When $\rho L$ is normalized by the central density $\rho_{part}(0,0) = \rho_{cent}$, then $S_{loss}$ ($R_{AA}$) become universal in

the quantities $\rho L / \rho_{cent}$ for both $p_T$ ranges with a linear dependence. The universality appears to become more exact in the higher $p_T$ range. A similar improvement (not shown) of the qualitative universality for $\rho L^2$ and $\rho L_{xy}$ is also observed when these quantities are scaled in the same way by $\rho_{cent}$. The fact that scaling by $\rho_{cent}$ improves the universality suggests that simple geometry may be more important than the details of the participant density.

The most important of these observations is the absence of suppression for the same value of $L_\varepsilon \leqslant 2$ fm for both $p_T$ ranges, $3 \leqslant p_T \leqslant 5$ GeV/$c$ and $5 \leqslant p_T \leqslant 8$ GeV/$c$. This may suggest a "formation time effect" (see Ref. [58], also considering mechanisms suggested in Ref. [60]) or some other type of emission zone which has generally not been taken into account in parton energy-loss models. The level of universal scaling with this simple geometric quantity is surprising.
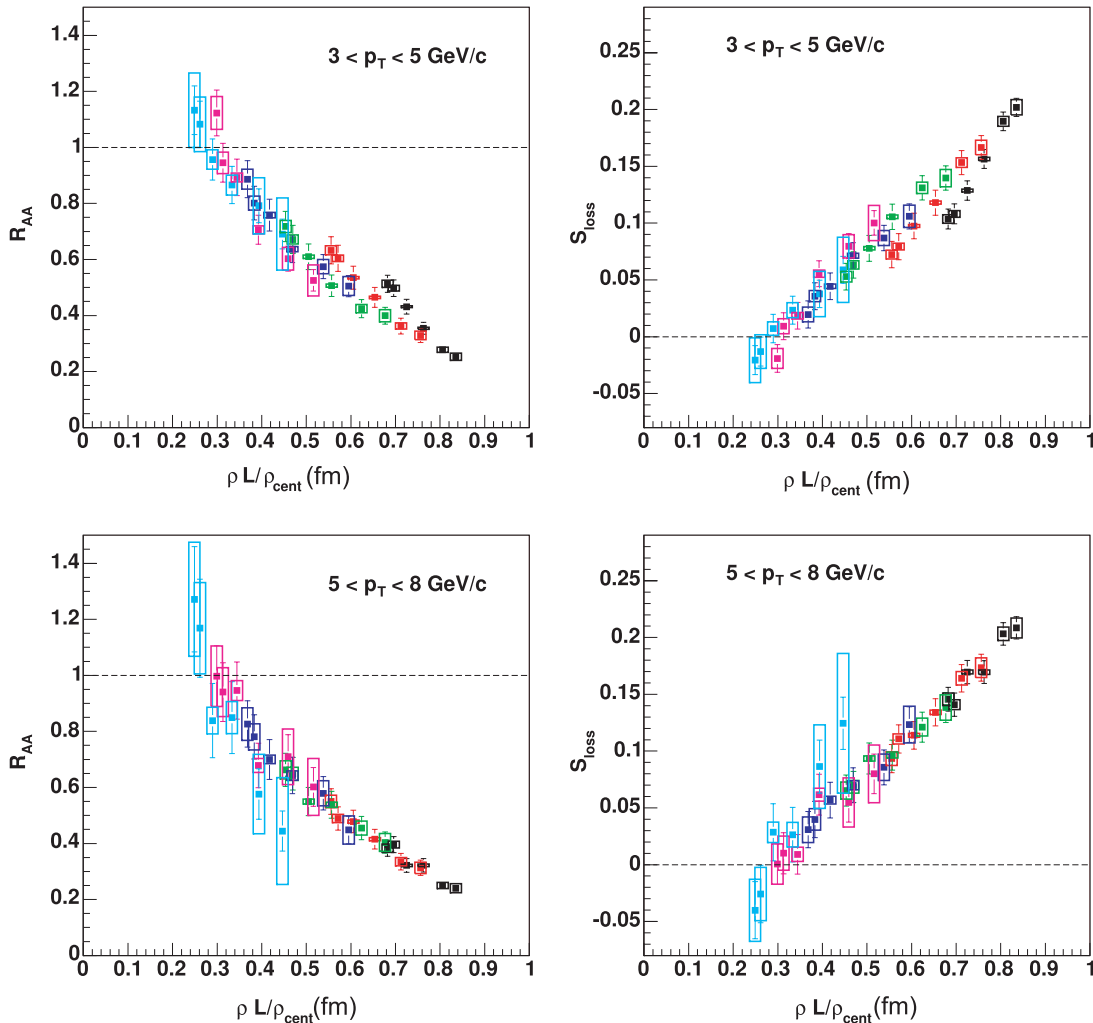
FIG. 21. (Color online) $R_{AA}$ and $S_{loss}$ versus $\rho L$ normalized by the most central ($b_x = b_y = 0$) density $\rho_{cent}$. Colors/data points as in Fig. 17.

## V. SUMMARY AND CONCLUSIONS

We have presented a detailed analysis of high-$p_T$ neutral pion suppression as a function of transverse momentum, centrality, and angle with respect to reaction plane in Au+Au collisions at $\sqrt{s_{NN}} = 200$ GeV. The $\pi^0$ yields have been measured in the range $p_T \approx 1$–14 GeV/$c$ in nine centrality bins and compared to the $\pi^0$ differential cross sections measured in $p+p$. The ratio of Au+Au over $p+p$ spectra (scaled by the number of equivalent nucleon-nucleon scatterings) is reduced more and more for larger centralities. The resulting suppression factor is, however, independent of $p_T$ above $p_T \approx 4$ GeV/$c$ for all centralities. This observation can be interpreted as an indication of a constant effective fractional energy loss, fixed $S_{loss}$ "$p_T$ shift," in the Au+Au compared to the $p+p$ yields. The dependence of $S_{loss}$ in the centrality as given by the number of participating nucleons $N_{part}$ follows an approximately $N_{part}^{2/3}$ law as predicted by parton energy loss models.

To constrain the "jet quenching" models with more differential observables, we have experimentally tested the path-length ($L$) dependence of the energy loss by exploiting the spatial azimuthal asymmetry of the system produced in noncentral nuclear collisions. Due to the characteristic almondlike shape of the overlapping matter produced in $A+A$ reactions with finite impact parameter, partons traversing the produced medium along the direction perpendicular to the reaction plane ("out-of-plane") will comparatively go through more matter than those going parallel to it ("in-plane") and therefore are expected to lose more energy.

We have studied the suppression pattern along different $\Delta\phi$ trajectories with respect to the reaction plane determined with the beam-beam counters at high rapidities. The measured $R_{AA}(\Delta\phi)$ curves show clearly a factor of $\sim$2 more suppression out-of-plane ($\Delta\phi = \pi/2$) than in-plane ($\Delta\phi = 0$) for all the centralities (eccentricities) considered. Theoretical calculations of parton energy loss in an azimuthally asymmetric medium predict a significantly smaller difference between the suppression patterns for partons emitted at $\Delta\phi = 0$ and $\Delta\phi = \pi/2$ [29,32,33]. The discrepancy is stronger for more peripheral centralities (with correspondingly larger eccentricities) and challenges the underlying in-medium path-length

dependence of non-Abelian parton energy loss. Although elliptic flow effects are responsible for extra boost of in-plane (compared to out-of-plane) pions, it is unclear how such collective effects persist up to $p_T$ values as high as $\sim 8$ GeV/$c$. We have analyzed the observed reaction-plane and centrality dependence of the nuclear modification factor with three different versions of a Monte Carlo model with an increasing level of refinement in the description of the azimuthal propagation of the parton in the medium. For all three approaches we observe that the $\pi^0$ suppression tends to vanish for values of the path-length $L \approx 2$ fm in the two $p_T$ ranges considered, $3 \leqslant p_T \leqslant 5$ GeV/$c$ and $5 \leqslant p_T \leqslant 8$ GeV/$c$. Such a result suggests either a formation time effect or a surface emission zone that results in a $p_T$-independent suppression and puts additional constraints to parton energy-loss models.

### APPENDIX: DATA TABLES OF AU + AU $\rightarrow \pi^0 + X$ $p_T$ SPECTRA

Tables IV–XVI show numerical data in the same units as plotted in the figures: $p_T$ (GeV/$c$) and invariant yield ($c^2$/GeV$^2$).

TABLE IV. Final combined PbSc+PbGl $\pi^0$ invariant yields vs. $p_T$ for centrality 0–10%.

| $p_T$ | Yield | Stat. error | % | Sys. error | % |
|---|---|---|---|---|---|
| 1.25 | 3.314 | $2.518\times10^{-2}$ | 0.76 | $4.026\times10^{-1}$ | 12.15 |
| 1.75 | $5.981\times10^{-1}$ | $4.946\times10^{-3}$ | 0.83 | $6.784\times10^{-2}$ | 11.34 |
| 2.25 | $1.208\times10^{-1}$ | $1.253\times10^{-3}$ | 1.04 | $1.447\times10^{-2}$ | 11.98 |
| 2.75 | $2.718\times10^{-2}$ | $3.744\times10^{-4}$ | 1.38 | $3.521\times10^{-3}$ | 12.96 |
| 3.25 | $6.970\times10^{-3}$ | $1.270\times10^{-4}$ | 1.82 | $9.751\times10^{-4}$ | 13.99 |
| 3.75 | $2.158\times10^{-3}$ | $4.713\times10^{-5}$ | 2.18 | $2.686\times10^{-4}$ | 12.44 |
| 4.25 | $7.185\times10^{-4}$ | $2.133\times10^{-5}$ | 2.97 | $9.349\times10^{-5}$ | 13.01 |
| 4.75 | $2.715\times10^{-4}$ | $1.063\times10^{-5}$ | 3.92 | $3.575\times10^{-5}$ | 13.17 |
| 5.25 | $1.288\times10^{-4}$ | $5.931\times10^{-6}$ | 4.61 | $1.702\times10^{-5}$ | 13.21 |
| 5.75 | $5.417\times10^{-5}$ | $2.606\times10^{-6}$ | 4.81 | $7.731\times10^{-6}$ | 14.27 |
| 6.25 | $2.940\times10^{-5}$ | $1.560\times10^{-6}$ | 5.31 | $4.106\times10^{-6}$ | 13.97 |
| 6.75 | $1.280\times10^{-5}$ | $9.501\times10^{-7}$ | 7.43 | $1.922\times10^{-6}$ | 15.02 |
| 7.25 | $7.641\times10^{-6}$ | $6.459\times10^{-7}$ | 8.45 | $1.241\times10^{-6}$ | 16.24 |
| 7.75 | $4.630\times10^{-6}$ | $4.668\times10^{-7}$ | 10.08 | $7.508\times10^{-7}$ | 16.22 |
| 8.50 | $1.883\times10^{-6}$ | $1.809\times10^{-7}$ | 9.61 | $3.033\times10^{-7}$ | 16.11 |
| 9.50 | $1.057\times10^{-6}$ | $1.276\times10^{-7}$ | 12.07 | $1.952\times10^{-7}$ | 18.47 |
| 11.00 | $2.777\times10^{-7}$ | $4.274\times10^{-8}$ | 15.39 | $5.664\times10^{-8}$ | 20.39 |
| 13.00 | $5.941\times10^{-8}$ | $1.704\times10^{-8}$ | 28.87 | $1.222\times10^{-8}$ | 20.57 |

TABLE V. Final combined PbSc+PbGl $\pi^0$ invariant yields vs. $p_T$ for centrality 10–20%.

| $p_T$ | Yield | Stat. error | % | Sys. error | % |
|---|---|---|---|---|---|
| 1.25 | 2.054 | $1.461\times10^{-2}$ | 0.71 | $2.655\times10^{-1}$ | 12.93 |
| 1.75 | $4.137\times10^{-1}$ | $2.933\times10^{-3}$ | 0.71 | $4.616\times10^{-2}$ | 11.16 |
| 2.25 | $8.576\times10^{-2}$ | $7.654\times10^{-4}$ | 0.89 | $1.039\times10^{-2}$ | 12.11 |
| 2.75 | $2.028\times10^{-2}$ | $2.305\times10^{-4}$ | 1.14 | $2.612\times10^{-3}$ | 12.88 |
| 3.25 | $5.057\times10^{-3}$ | $7.980\times10^{-5}$ | 1.58 | $6.778\times10^{-4}$ | 13.40 |
| 3.75 | $1.665\times10^{-3}$ | $3.170\times10^{-5}$ | 1.90 | $1.995\times10^{-4}$ | 11.98 |
| 4.25 | $5.859\times10^{-4}$ | $1.511\times10^{-5}$ | 2.58 | $7.301\times10^{-5}$ | 12.46 |
| 4.75 | $2.253\times10^{-4}$ | $7.948\times10^{-6}$ | 3.53 | $3.003\times10^{-5}$ | 13.33 |
| 5.25 | $9.486\times10^{-5}$ | $4.369\times10^{-6}$ | 4.61 | $1.246\times10^{-5}$ | 13.14 |
| 5.75 | $4.651\times10^{-5}$ | $2.087\times10^{-6}$ | 4.49 | $6.696\times10^{-6}$ | 14.40 |
| 6.25 | $2.224\times10^{-5}$ | $1.249\times10^{-6}$ | 5.62 | $3.252\times10^{-6}$ | 14.62 |
| 6.75 | $1.109\times10^{-5}$ | $8.621\times10^{-7}$ | 7.78 | $1.899\times10^{-6}$ | 17.13 |
| 7.25 | $6.455\times10^{-6}$ | $5.485\times10^{-7}$ | 8.50 | $1.091\times10^{-6}$ | 16.90 |
| 7.75 | $3.568\times10^{-6}$ | $3.999\times10^{-7}$ | 11.21 | $7.173\times10^{-7}$ | 20.10 |
| 8.50 | $1.724\times10^{-6}$ | $1.718\times10^{-7}$ | 9.96 | $3.279\times10^{-7}$ | 19.01 |
| 9.50 | $6.318\times10^{-7}$ | $9.789\times10^{-8}$ | 15.49 | $1.144\times10^{-7}$ | 18.11 |
| 11.00 | $1.701\times10^{-7}$ | $3.347\times10^{-8}$ | 19.68 | $3.147\times10^{-8}$ | 18.51 |
| 13.00 | $5.093\times10^{-8}$ | $1.610\times10^{-8}$ | 31.62 | $9.747\times10^{-9}$ | 19.14 |

TABLE VI. Final combined PbSc+PbGl $\pi^0$ invariant yields vs. $p_T$ for centrality 20–30%.

| $p_T$ | Yield | Stat. error | % | Sys. error | % |
|---|---|---|---|---|---|
| 1.25 | 1.601 | $9.668\times10^{-3}$ | 0.60 | $1.852\times10^{-1}$ | 11.57 |
| 1.75 | $2.879\times10^{-1}$ | $1.911\times10^{-3}$ | 0.66 | $3.260\times10^{-2}$ | 11.32 |
| 2.25 | $6.045\times10^{-2}$ | $5.117\times10^{-4}$ | 0.85 | $7.416\times10^{-3}$ | 12.27 |
| 2.75 | $1.429\times10^{-2}$ | $1.537\times10^{-4}$ | 1.08 | $1.761\times10^{-3}$ | 12.32 |
| 3.25 | $3.983\times10^{-3}$ | $5.534\times10^{-5}$ | 1.39 | $5.192\times10^{-4}$ | 13.04 |
| 3.75 | $1.233\times10^{-3}$ | $2.340\times10^{-5}$ | 1.90 | $1.546\times10^{-4}$ | 12.53 |
| 4.25 | $4.749\times10^{-4}$ | $1.158\times10^{-5}$ | 2.44 | $6.115\times10^{-5}$ | 12.88 |
| 4.75 | $1.732\times10^{-4}$ | $5.898\times10^{-6}$ | 3.41 | $2.258\times10^{-5}$ | 13.04 |
| 5.25 | $7.761\times10^{-5}$ | $3.503\times10^{-6}$ | 4.51 | $1.074\times10^{-5}$ | 13.84 |
| 5.75 | $3.573\times10^{-5}$ | $1.627\times10^{-6}$ | 4.55 | $4.870\times10^{-6}$ | 13.63 |
| 6.25 | $1.714\times10^{-5}$ | $9.568\times10^{-7}$ | 5.58 | $2.389\times10^{-6}$ | 13.94 |
| 6.75 | $9.015\times10^{-6}$ | $6.625\times10^{-7}$ | 7.35 | $1.384\times10^{-6}$ | 15.36 |
| 7.25 | $5.146\times10^{-6}$ | $4.423\times10^{-7}$ | 8.59 | $8.214\times10^{-7}$ | 15.96 |
| 7.75 | $2.878\times10^{-6}$ | $3.267\times10^{-7}$ | 11.35 | $5.465\times10^{-7}$ | 18.99 |
| 8.50 | $1.363\times10^{-6}$ | $1.452\times10^{-7}$ | 10.65 | $2.517\times10^{-7}$ | 18.46 |
| 9.50 | $6.216\times10^{-7}$ | $8.347\times10^{-8}$ | 13.43 | $1.088\times10^{-7}$ | 17.50 |
| 11.00 | $1.825\times10^{-7}$ | $2.972\times10^{-8}$ | 16.28 | $3.299\times10^{-8}$ | 18.08 |
| 13.00 | $3.552\times10^{-8}$ | $1.267\times10^{-8}$ | 35.68 | $6.852\times10^{-9}$ | 19.29 |

TABLE VII. Final combined PbSc+PbGl $\pi^0$ invariant yields vs. $p_T$ for centrality 30–40%.

| $p_T$ | Yield | Stat. error | % | Sys. error | % |
|---|---|---|---|---|---|
| 1.25 | 1.040 | $5.648\times10^{-3}$ | 0.54 | $1.244\times10^{-1}$ | 11.96 |
| 1.75 | $1.754\times10^{-1}$ | $1.100\times10^{-3}$ | 0.63 | $2.001\times10^{-2}$ | 11.41 |
| 2.25 | $3.833\times10^{-2}$ | $3.102\times10^{-4}$ | 0.81 | $4.567\times10^{-3}$ | 11.91 |
| 2.75 | $9.610\times10^{-3}$ | $9.930\times10^{-5}$ | 1.03 | $1.175\times10^{-3}$ | 12.23 |
| 3.25 | $2.670\times10^{-3}$ | $3.764\times10^{-5}$ | 1.41 | $3.512\times10^{-4}$ | 13.15 |
| 3.75 | $8.612\times10^{-4}$ | $1.667\times10^{-5}$ | 1.94 | $1.097\times10^{-4}$ | 12.74 |
| 4.25 | $3.270\times10^{-4}$ | $8.158\times10^{-6}$ | 2.49 | $4.185\times10^{-5}$ | 12.80 |
| 4.75 | $1.252\times10^{-4}$ | $4.421\times10^{-6}$ | 3.53 | $1.619\times10^{-5}$ | 12.94 |
| 5.25 | $5.266\times10^{-5}$ | $2.822\times10^{-6}$ | 5.36 | $7.394\times10^{-6}$ | 14.04 |
| 5.75 | $2.761\times10^{-5}$ | $1.348\times10^{-6}$ | 4.88 | $3.839\times10^{-6}$ | 13.90 |
| 6.25 | $1.189\times10^{-5}$ | $8.138\times10^{-7}$ | 6.85 | $1.949\times10^{-6}$ | 16.39 |
| 6.75 | $7.115\times10^{-6}$ | $5.804\times10^{-7}$ | 8.16 | $1.198\times10^{-6}$ | 16.84 |
| 7.25 | $3.705\times10^{-6}$ | $3.972\times10^{-7}$ | 10.72 | $6.264\times10^{-7}$ | 16.91 |
| 7.75 | $1.898\times10^{-6}$ | $2.549\times10^{-7}$ | 13.42 | $3.307\times10^{-7}$ | 17.42 |
| 8.50 | $1.168\times10^{-6}$ | $1.301\times10^{-7}$ | 11.13 | $1.967\times10^{-7}$ | 16.83 |
| 9.50 | $5.043\times10^{-7}$ | $8.312\times10^{-8}$ | 16.48 | $9.634\times10^{-8}$ | 19.10 |
| 11.00 | $1.541\times10^{-7}$ | $2.748\times10^{-8}$ | 17.83 | $2.910\times10^{-8}$ | 18.89 |
| 13.00 | $2.941\times10^{-8}$ | $1.278\times10^{-8}$ | 33.46 | $5.621\times10^{-9}$ | 19.11 |

TABLE VIII. Final combined PbSc+PbGl $\pi^0$ invariant yields vs. $p_T$ for centrality 40–50%.

| $p_T$ | Yield | Stat. error | % | Sys. error | % |
|---|---|---|---|---|---|
| 1.25 | $6.389\times10^{-1}$ | $3.367\times10^{-3}$ | 0.53 | $7.216\times10^{-2}$ | 11.29 |
| 1.75 | $1.156\times10^{-1}$ | $6.789\times10^{-4}$ | 0.59 | $1.315\times10^{-2}$ | 11.37 |
| 2.25 | $2.442\times10^{-2}$ | $1.926\times10^{-4}$ | 0.79 | $2.911\times10^{-3}$ | 11.92 |
| 2.75 | $6.172\times10^{-3}$ | $6.521\times10^{-5}$ | 1.06 | $7.890\times10^{-4}$ | 12.78 |
| 3.25 | $1.682\times10^{-3}$ | $2.455\times10^{-5}$ | 1.46 | $2.194\times10^{-4}$ | 13.04 |
| 3.75 | $5.822\times10^{-4}$ | $1.161\times10^{-5}$ | 1.99 | $7.179\times10^{-5}$ | 12.33 |
| 4.25 | $1.927\times10^{-4}$ | $6.113\times10^{-6}$ | 3.17 | $2.480\times10^{-5}$ | 12.87 |
| 4.75 | $8.818\times10^{-5}$ | $3.476\times10^{-6}$ | 3.94 | $1.169\times10^{-5}$ | 13.26 |
| 5.25 | $3.627\times10^{-5}$ | $2.166\times10^{-6}$ | 5.97 | $4.995\times10^{-6}$ | 13.77 |
| 5.75 | $1.611\times10^{-5}$ | $9.656\times10^{-7}$ | 5.99 | $2.261\times10^{-6}$ | 14.04 |
| 6.25 | $9.635\times10^{-6}$ | $6.880\times10^{-7}$ | 7.14 | $1.490\times10^{-6}$ | 15.47 |
| 6.75 | $4.467\times10^{-6}$ | $4.278\times10^{-7}$ | 9.58 | $7.232\times10^{-7}$ | 16.19 |
| 7.25 | $2.044\times10^{-6}$ | $2.585\times10^{-7}$ | 12.65 | $3.197\times10^{-7}$ | 15.64 |
| 7.75 | $1.363\times10^{-6}$ | $2.198\times10^{-7}$ | 16.13 | $2.882\times10^{-7}$ | 21.15 |
| 8.50 | $7.878\times10^{-7}$ | $1.056\times10^{-7}$ | 13.41 | $1.409\times10^{-7}$ | 17.88 |
| 9.50 | $2.197\times10^{-7}$ | $5.630\times10^{-8}$ | 25.62 | $4.969\times10^{-8}$ | 22.61 |
| 11.00 | $1.053\times10^{-7}$ | $2.280\times10^{-8}$ | 21.66 | $2.116\times10^{-8}$ | 20.10 |
| 13.00 | $2.792\times10^{-8}$ | $1.140\times10^{-8}$ | 40.82 | $6.121\times10^{-9}$ | 21.92 |

TABLE IX. Final combined PbSc+PbGl $\pi^0$ invariant yields vs. $p_T$ for centrality 50–60%. For points with no errors given, data value represents 90% confidence level upper limit.

| $p_T$ | Yield | Stat. error | % | Sys. error | % |
|---|---|---|---|---|---|
| 1.25 | $3.593\times10^{-1}$ | $1.941\times10^{-3}$ | 0.54 | $4.022\times10^{-2}$ | 11.19 |
| 1.75 | $6.197\times10^{-2}$ | $4.018\times10^{-4}$ | 0.65 | $7.069\times10^{-3}$ | 11.41 |
| 2.25 | $1.309\times10^{-2}$ | $1.175\times10^{-4}$ | 0.90 | $1.553\times10^{-3}$ | 11.87 |
| 2.75 | $3.479\times10^{-3}$ | $4.211\times10^{-5}$ | 1.21 | $4.205\times10^{-4}$ | 12.09 |
| 3.25 | $1.019\times10^{-3}$ | $1.695\times10^{-5}$ | 1.66 | $1.291\times10^{-4}$ | 12.67 |
| 3.75 | $3.480\times10^{-4}$ | $8.518\times10^{-6}$ | 2.45 | $4.380\times10^{-5}$ | 12.59 |
| 4.25 | $1.329\times10^{-4}$ | $4.558\times10^{-6}$ | 3.43 | $1.763\times10^{-5}$ | 13.26 |
| 4.75 | $4.959\times10^{-5}$ | $2.434\times10^{-6}$ | 4.91 | $6.310\times10^{-6}$ | 12.73 |
| 5.25 | $2.125\times10^{-5}$ | $1.585\times10^{-6}$ | 7.46 | $3.032\times10^{-6}$ | 14.27 |
| 5.75 | $9.917\times10^{-6}$ | $7.569\times10^{-7}$ | 7.63 | $1.540\times10^{-6}$ | 15.52 |
| 6.25 | $6.127\times10^{-6}$ | $5.471\times10^{-7}$ | 8.93 | $9.978\times10^{-7}$ | 16.29 |
| 6.75 | $3.246\times10^{-6}$ | $3.392\times10^{-7}$ | 10.45 | $4.965\times10^{-7}$ | 15.30 |
| 7.25 | $1.664\times10^{-6}$ | $2.449\times10^{-7}$ | 14.72 | $3.102\times10^{-7}$ | 18.65 |
| 7.75 | $1.129\times10^{-6}$ | $1.886\times10^{-7}$ | 16.70 | $2.114\times10^{-7}$ | 18.72 |
| 8.50 | $3.362\times10^{-7}$ | $7.419\times10^{-8}$ | 22.07 | $6.694\times10^{-8}$ | 19.91 |
| 9.50 | $1.817\times10^{-7}$ | $4.619\times10^{-8}$ | 25.42 | $3.329\times10^{-8}$ | 18.32 |
| 11.00 | $2.858\times10^{-8}$ | $1.112\times10^{-8}$ | 38.89 | $4.803\times10^{-9}$ | 16.81 |
| 13.00 | $2.311\times10^{-8}$ | — | — | — | — |

TABLE X. Final combined PbSc+PbGl $\pi^0$ invariant yields vs. $p_T$ for centrality 60–70%.

| $p_T$ | Yield | Stat. error | % | Sys. error | % |
|---|---|---|---|---|---|
| 1.25 | $1.731\times10^{-1}$ | $1.121\times10^{-3}$ | 0.65 | $1.985\times10^{-2}$ | 11.47 |
| 1.75 | $3.022\times10^{-2}$ | $2.288\times10^{-4}$ | 0.76 | $3.425\times10^{-3}$ | 11.33 |
| 2.25 | $6.567\times10^{-3}$ | $7.011\times10^{-5}$ | 1.07 | $7.773\times10^{-4}$ | 11.84 |
| 2.75 | $1.644\times10^{-3}$ | $2.565\times10^{-5}$ | 1.56 | $2.057\times10^{-4}$ | 12.51 |
| 3.25 | $5.255\times10^{-4}$ | $1.158\times10^{-5}$ | 2.20 | $6.682\times10^{-5}$ | 12.72 |
| 3.75 | $1.801\times10^{-4}$ | $6.044\times10^{-6}$ | 3.36 | $2.259\times10^{-5}$ | 12.54 |
| 4.25 | $6.986\times10^{-5}$ | $3.184\times10^{-6}$ | 4.56 | $9.254\times10^{-6}$ | 13.25 |
| 4.75 | $2.312\times10^{-5}$ | $1.631\times10^{-6}$ | 7.06 | $3.101\times10^{-6}$ | 13.41 |
| 5.25 | $1.156\times10^{-5}$ | $1.145\times10^{-6}$ | 9.90 | $1.720\times10^{-6}$ | 14.87 |
| 5.75 | $4.884\times10^{-6}$ | $5.045\times10^{-7}$ | 10.33 | $7.560\times10^{-7}$ | 15.48 |
| 6.25 | $2.690\times10^{-6}$ | $3.650\times10^{-7}$ | 13.57 | $4.303\times10^{-7}$ | 16.00 |
| 6.75 | $1.822\times10^{-6}$ | $2.658\times10^{-7}$ | 14.58 | $3.369\times10^{-7}$ | 18.48 |
| 7.25 | $6.281\times10^{-7}$ | $1.480\times10^{-7}$ | 23.57 | $1.178\times10^{-7}$ | 18.76 |
| 7.75 | $2.446\times10^{-7}$ | $1.082\times10^{-7}$ | 44.22 | $4.632\times10^{-8}$ | 18.94 |
| 8.50 | $1.417\times10^{-7}$ | $4.482\times10^{-8}$ | 31.62 | $2.707\times10^{-8}$ | 19.10 |
| 9.50 | $1.094\times10^{-7}$ | $3.843\times10^{-8}$ | 35.14 | $2.106\times10^{-8}$ | 19.26 |
| 11.00 | $2.492\times10^{-8}$ | $1.114\times10^{-8}$ | 44.72 | $4.816\times10^{-9}$ | 19.33 |
| 13.00 | $4.728\times10^{-9}$ | $4.728\times10^{-9}$ | 100.00 | $9.226\times10^{-10}$ | 19.51 |

TABLE XI. Final combined PbSc+PbGl $\pi^0$ invariant yields vs. $p_T$ for centrality 70–80%.

| $p_T$ | Yield | Stat. error | % | Sys. error | % |
|---|---|---|---|---|---|
| 1.25 | $7.416\times10^{-2}$ | $5.166\times10^{-4}$ | 0.70 | $8.842\times10^{-3}$ | 11.92 |
| 1.75 | $1.282\times10^{-2}$ | $1.189\times10^{-4}$ | 0.93 | $1.496\times10^{-3}$ | 11.67 |
| 2.25 | $2.721\times10^{-3}$ | $3.774\times10^{-5}$ | 1.39 | $3.245\times10^{-4}$ | 11.92 |
| 2.75 | $7.455\times10^{-4}$ | $1.514\times10^{-5}$ | 2.03 | $9.131\times10^{-5}$ | 12.25 |
| 3.25 | $2.461\times10^{-4}$ | $7.508\times10^{-6}$ | 3.05 | $3.248\times10^{-5}$ | 13.20 |
| 3.75 | $7.200\times10^{-5}$ | $3.689\times10^{-6}$ | 5.12 | $9.687\times10^{-6}$ | 13.46 |
| 4.25 | $2.609\times10^{-5}$ | $2.071\times10^{-6}$ | 7.94 | $4.034\times10^{-6}$ | 15.46 |
| 4.75 | $1.288\times10^{-5}$ | $1.308\times10^{-6}$ | 10.15 | $2.161\times10^{-6}$ | 16.78 |
| 5.25 | $4.650\times10^{-6}$ | $7.727\times10^{-7}$ | 16.62 | $9.050\times10^{-7}$ | 19.46 |
| 5.75 | $2.416\times10^{-6}$ | $3.897\times10^{-7}$ | 16.13 | $4.736\times10^{-7}$ | 19.60 |
| 6.25 | $1.763\times10^{-6}$ | $2.713\times10^{-7}$ | 15.39 | $2.795\times10^{-7}$ | 15.85 |
| 6.75 | $5.945\times10^{-7}$ | $1.651\times10^{-7}$ | 27.77 | $1.221\times10^{-7}$ | 20.53 |
| 7.25 | $4.817\times10^{-7}$ | $1.245\times10^{-7}$ | 25.84 | $8.088\times10^{-8}$ | 16.79 |
| 7.75 | $1.344\times10^{-7}$ | $6.718\times10^{-8}$ | 50.00 | $2.545\times10^{-8}$ | 18.94 |
| 8.50 | $1.135\times10^{-7}$ | $4.012\times10^{-8}$ | 35.36 | $2.167\times10^{-8}$ | 19.10 |
| 9.50 | $4.968\times10^{-8}$ | $2.484\times10^{-8}$ | 50.00 | $9.568\times10^{-9}$ | 19.26 |
| 11.00 | $5.060\times10^{-9}$ | $5.060\times10^{-9}$ | 100.00 | $9.778\times10^{-10}$ | 19.33 |

TABLE XII. Final combined PbSc+PbGl $\pi^0$ invariant yields vs. $p_T$ for centrality 80–92%.

| $p_T$ | Yield | Stat. error | % | Sys. error | % |
|---|---|---|---|---|---|
| 1.25 | $3.494\times10^{-2}$ | $6.093\times10^{-4}$ | 1.74 | $4.504\times10^{-3}$ | 12.89 |
| 1.75 | $6.037\times10^{-3}$ | $1.291\times10^{-4}$ | 2.14 | $7.607\times10^{-4}$ | 12.60 |
| 2.25 | $1.319\times10^{-3}$ | $3.628\times10^{-5}$ | 2.75 | $1.701\times10^{-4}$ | 12.89 |
| 2.75 | $3.321\times10^{-4}$ | $1.243\times10^{-5}$ | 3.74 | $4.570\times10^{-5}$ | 13.76 |
| 3.25 | $1.059\times10^{-4}$ | $5.281\times10^{-6}$ | 4.99 | $1.483\times10^{-5}$ | 14.01 |
| 3.75 | $3.625\times10^{-5}$ | $2.408\times10^{-6}$ | 6.64 | $4.455\times10^{-6}$ | 12.29 |
| 4.25 | $1.233\times10^{-5}$ | $1.293\times10^{-6}$ | 10.48 | $1.730\times10^{-6}$ | 14.03 |
| 4.75 | $6.501\times10^{-6}$ | $7.988\times10^{-7}$ | 12.29 | $9.044\times10^{-7}$ | 13.91 |
| 5.25 | $3.018\times10^{-6}$ | $5.360\times10^{-7}$ | 17.76 | $4.224\times10^{-7}$ | 13.99 |
| 5.75 | $1.072\times10^{-6}$ | $2.315\times10^{-7}$ | 21.60 | $1.815\times10^{-7}$ | 16.94 |
| 6.25 | $3.265\times10^{-7}$ | $1.154\times10^{-7}$ | 35.36 | $5.945\times10^{-8}$ | 18.21 |
| 6.75 | $2.805\times10^{-7}$ | $9.918\times10^{-8}$ | 35.36 | $5.185\times10^{-8}$ | 18.48 |
| 7.25 | $2.231\times10^{-7}$ | $8.434\times10^{-8}$ | 37.80 | $4.187\times10^{-8}$ | 18.76 |
| 7.75 | $8.467\times10^{-8}$ | $4.888\times10^{-8}$ | 57.74 | $1.604\times10^{-8}$ | 18.94 |
| 8.50 | $3.602\times10^{-8}$ | $2.080\times10^{-8}$ | 57.74 | $6.880\times10^{-9}$ | 19.10 |
| 9.50 | $1.077\times10^{-8}$ | $1.077\times10^{-8}$ | 100.00 | $2.074\times10^{-9}$ | 19.26 |
| 11.00 | $4.375\times10^{-9}$ | $4.375\times10^{-9}$ | 100.00 | $8.455\times10^{-10}$ | 19.32 |

TABLE XIII. Final combined PbSc+PbGl $\pi^0$ invariant yields vs. $p_T$ for centrality 0–92%.

| $p_T$ | Yield | Stat. error | % | Sys. error | % |
|---|---|---|---|---|---|
| 1.25 | 1.078 | $3.333\times10^{-3}$ | 0.31 | $1.205\times10^{-1}$ | 11.17 |
| 1.75 | $1.928\times10^{-1}$ | $6.847\times10^{-4}$ | 0.36 | $2.171\times10^{-2}$ | 11.26 |
| 2.25 | $4.038\times10^{-2}$ | $1.742\times10^{-4}$ | 0.43 | $4.822\times10^{-3}$ | 11.94 |
| 2.75 | $9.578\times10^{-3}$ | $5.293\times10^{-5}$ | 0.55 | $1.202\times10^{-3}$ | 12.55 |
| 3.25 | $2.564\times10^{-3}$ | $1.858\times10^{-5}$ | 0.72 | $3.375\times10^{-4}$ | 13.17 |
| 3.75 | $8.115\times10^{-4}$ | $7.353\times10^{-6}$ | 0.91 | $1.013\times10^{-4}$ | 12.48 |
| 4.25 | $2.906\times10^{-4}$ | $3.475\times10^{-6}$ | 1.20 | $3.729\times10^{-5}$ | 12.84 |
| 4.75 | $1.121\times10^{-4}$ | $1.806\times10^{-6}$ | 1.61 | $1.466\times10^{-5}$ | 13.08 |
| 5.25 | $4.924\times10^{-5}$ | $1.031\times10^{-6}$ | 2.09 | $6.494\times10^{-6}$ | 13.19 |
| 5.75 | $2.240\times10^{-5}$ | $4.723\times10^{-7}$ | 2.11 | $3.012\times10^{-6}$ | 13.45 |
| 6.25 | $1.190\times10^{-5}$ | $2.909\times10^{-7}$ | 2.44 | $1.647\times10^{-6}$ | 13.83 |
| 6.75 | $5.970\times10^{-6}$ | $1.943\times10^{-7}$ | 3.25 | $8.494\times10^{-7}$ | 14.23 |
| 7.25 | $3.246\times10^{-6}$ | $1.273\times10^{-7}$ | 3.92 | $4.758\times10^{-7}$ | 14.65 |
| 7.75 | $1.715\times10^{-6}$ | $9.049\times10^{-8}$ | 5.28 | $2.658\times10^{-7}$ | 15.49 |
| 8.50 | $8.583\times10^{-7}$ | $3.892\times10^{-8}$ | 4.53 | $1.285\times10^{-7}$ | 14.98 |
| 9.50 | $3.078\times10^{-7}$ | $2.351\times10^{-8}$ | 7.64 | $5.041\times10^{-8}$ | 16.38 |
| 11.00 | $9.178\times10^{-8}$ | $7.770\times10^{-9}$ | 8.47 | $1.417\times10^{-8}$ | 15.44 |
| 13.00 | $2.380\times10^{-8}$ | $3.856\times10^{-9}$ | 16.20 | $3.816\times10^{-9}$ | 16.03 |

TABLE XV. $\pi^0$ spectrum for combined centralities: 20–60%

| $p_T$ | Yield | Stat. error | % | Sys. error | % |
|---|---|---|---|---|---|
| 1.25 | $9.097\times10^{-1}$ | $2.963\times10^{-3}$ | 0.33 | $9.041\times10^{-2}$ | 9.94 |
| 1.75 | $1.602\times10^{-1}$ | $5.854\times10^{-4}$ | 0.37 | $1.570\times10^{-2}$ | 9.80 |
| 2.25 | $3.407\times10^{-2}$ | $1.599\times10^{-4}$ | 0.47 | $3.579\times10^{-3}$ | 10.51 |
| 2.75 | $8.386\times10^{-3}$ | $4.969\times10^{-5}$ | 0.59 | $9.138\times10^{-4}$ | 10.90 |
| 3.25 | $2.339\times10^{-3}$ | $1.832\times10^{-5}$ | 0.78 | $2.711\times10^{-4}$ | 11.59 |
| 3.75 | $7.562\times10^{-4}$ | $8.034\times10^{-6}$ | 1.06 | $8.387\times10^{-5}$ | 11.09 |
| 4.25 | $2.819\times10^{-4}$ | $4.021\times10^{-6}$ | 1.43 | $3.259\times10^{-5}$ | 11.56 |
| 4.75 | $1.090\times10^{-4}$ | $2.126\times10^{-6}$ | 1.95 | $1.263\times10^{-5}$ | 11.58 |
| 5.25 | $4.695\times10^{-5}$ | $1.310\times10^{-6}$ | 2.79 | $5.959\times10^{-6}$ | 12.69 |
| 5.75 | $2.234\times10^{-5}$ | $6.107\times10^{-7}$ | 2.73 | $2.907\times10^{-6}$ | 13.01 |
| 6.25 | $1.120\times10^{-5}$ | $3.833\times10^{-7}$ | 3.42 | $1.605\times10^{-6}$ | 14.33 |
| 6.75 | $5.961\times10^{-6}$ | $2.591\times10^{-7}$ | 4.35 | $8.809\times10^{-7}$ | 14.78 |
| 7.25 | $3.140\times10^{-6}$ | $1.732\times10^{-7}$ | 5.52 | $4.937\times10^{-7}$ | 15.73 |
| 7.75 | $1.817\times10^{-6}$ | $1.264\times10^{-7}$ | 6.96 | $3.292\times10^{-7}$ | 18.12 |
| 8.50 | $9.139\times10^{-7}$ | $5.846\times10^{-8}$ | 6.40 | $1.581\times10^{-7}$ | 17.30 |
| 9.50 | $3.818\times10^{-7}$ | $3.462\times10^{-8}$ | 9.07 | $7.055\times10^{-8}$ | 18.48 |
| 11.00 | $1.176\times10^{-7}$ | $1.194\times10^{-8}$ | 10.15 | $2.061\times10^{-8}$ | 17.52 |
| 13.00 | $2.899\times10^{-8}$ | $6.031\times10^{-9}$ | 20.80 | $4.497\times10^{-9}$ | 15.51 |

TABLE XIV. $\pi^0$ spectrum for combined centralities: 0–20%

| $p_T$ | Yield | Stat. error | % | Sys. error | % |
|---|---|---|---|---|---|
| 1.25 | 2.684 | $1.455\times10^{-2}$ | 0.54 | $3.106\times10^{-1}$ | 11.58 |
| 1.75 | $5.059\times10^{-1}$ | $2.875\times10^{-3}$ | 0.57 | $5.131\times10^{-2}$ | 10.14 |
| 2.25 | $1.033\times10^{-1}$ | $7.343\times10^{-4}$ | 0.71 | $1.137\times10^{-2}$ | 11.01 |
| 2.75 | $2.373\times10^{-2}$ | $2.198\times10^{-4}$ | 0.93 | $2.837\times10^{-3}$ | 11.96 |
| 3.25 | $6.014\times10^{-3}$ | $7.501\times10^{-5}$ | 1.25 | $7.693\times10^{-4}$ | 12.79 |
| 3.75 | $1.912\times10^{-3}$ | $2.840\times10^{-5}$ | 1.49 | $2.137\times10^{-4}$ | 11.18 |
| 4.25 | $6.522\times10^{-4}$ | $1.307\times10^{-5}$ | 2.00 | $7.660\times10^{-5}$ | 11.74 |
| 4.75 | $2.484\times10^{-4}$ | $6.637\times10^{-6}$ | 2.67 | $3.055\times10^{-5}$ | 12.30 |
| 5.25 | $1.118\times10^{-4}$ | $3.683\times10^{-6}$ | 3.29 | $1.368\times10^{-5}$ | 12.23 |
| 5.75 | $5.034\times10^{-5}$ | $1.670\times10^{-6}$ | 3.32 | $6.775\times10^{-6}$ | 13.46 |
| 6.25 | $2.582\times10^{-5}$ | $9.994\times10^{-7}$ | 3.87 | $3.466\times10^{-6}$ | 13.43 |
| 6.75 | $1.194\times10^{-5}$ | $6.415\times10^{-7}$ | 5.37 | $1.825\times10^{-6}$ | 15.29 |
| 7.25 | $7.048\times10^{-6}$ | $4.237\times10^{-7}$ | 6.01 | $1.115\times10^{-6}$ | 15.82 |
| 7.75 | $4.099\times10^{-6}$ | $3.073\times10^{-7}$ | 7.50 | $7.159\times10^{-7}$ | 17.46 |
| 8.50 | $1.804\times10^{-6}$ | $1.247\times10^{-7}$ | 6.92 | $3.037\times10^{-7}$ | 16.84 |
| 9.50 | $8.445\times10^{-7}$ | $8.042\times10^{-8}$ | 9.52 | $1.491\times10^{-7}$ | 17.65 |
| 11.00 | $2.239\times10^{-7}$ | $2.714\times10^{-8}$ | 12.12 | $4.219\times10^{-8}$ | 18.84 |
| 13.00 | $5.517\times10^{-8}$ | $1.011\times10^{-8}$ | 18.32 | $1.044\times10^{-8}$ | 18.93 |

TABLE XVI. $\pi^0$ spectrum for combined centralities: 60–92%

| $p_T$ | Yield | Stat. error | % | Sys. error | % |
|---|---|---|---|---|---|
| 1.25 | $9.037\times10^{-2}$ | $4.484\times10^{-4}$ | 0.50 | $9.891\times10^{-3}$ | 10.94 |
| 1.75 | $1.571\times10^{-2}$ | $9.400\times10^{-5}$ | 0.60 | $1.680\times10^{-3}$ | 10.69 |
| 2.25 | $3.397\times10^{-3}$ | $2.836\times10^{-5}$ | 0.83 | $3.765\times10^{-4}$ | 11.08 |
| 2.75 | $8.712\times10^{-4}$ | $1.041\times10^{-5}$ | 1.19 | $1.025\times10^{-4}$ | 11.76 |
| 3.25 | $2.808\times10^{-4}$ | $4.746\times10^{-6}$ | 1.69 | $3.442\times10^{-5}$ | 12.26 |
| 3.75 | $9.236\times10^{-5}$ | $2.390\times10^{-6}$ | 2.59 | $1.073\times10^{-5}$ | 11.61 |
| 4.25 | $3.461\times10^{-5}$ | $1.282\times10^{-6}$ | 3.70 | $4.593\times10^{-6}$ | 13.27 |
| 4.75 | $1.369\times10^{-5}$ | $7.188\times10^{-7}$ | 5.25 | $1.857\times10^{-6}$ | 13.57 |
| 5.25 | $6.198\times10^{-6}$ | $4.761\times10^{-7}$ | 7.68 | $9.308\times10^{-7}$ | 15.02 |
| 5.75 | $2.683\times10^{-6}$ | $2.173\times10^{-7}$ | 8.10 | $4.415\times10^{-7}$ | 16.46 |
| 6.25 | $1.514\times10^{-6}$ | $1.486\times10^{-7}$ | 9.81 | $2.414\times10^{-7}$ | 15.94 |
| 6.75 | $8.605\times10^{-7}$ | $1.046\times10^{-7}$ | 12.16 | $1.589\times10^{-7}$ | 18.46 |
| 7.25 | $4.305\times10^{-7}$ | $6.822\times10^{-8}$ | 15.85 | $7.426\times10^{-8}$ | 17.25 |
| 7.75 | $1.502\times10^{-7}$ | $4.381\times10^{-8}$ | 29.17 | $2.719\times10^{-8}$ | 18.10 |
| 8.50 | $9.326\times10^{-8}$ | $2.035\times10^{-8}$ | 21.82 | $1.706\times10^{-8}$ | 18.29 |
| 9.50 | $5.374\times10^{-8}$ | $1.486\times10^{-8}$ | 27.65 | $9.997\times10^{-9}$ | 18.60 |
| 11.00 | $1.101\times10^{-8}$ | $4.162\times10^{-9}$ | 37.80 | $2.062\times10^{-9}$ | 18.73 |
| 13.00 | $1.478\times10^{-9}$ | $1.478\times10^{-9}$ | 100.00 | $2.883\times10^{-10}$ | 19.51 |

[1] K. Adcox *et al.* (PHENIX), Phys. Rev. Lett. **89**, 212301 (2002).
[2] K. H. Ackermann *et al.* (STAR), Phys. Rev. Lett. **86**, 402 (2001).
[3] K. Adcox *et al.* (PHENIX), Phys. Rev. Lett. **88**, 022301 (2002).
[4] K. Adcox *et al.* (PHENIX), Phys. Lett. **B561**, 82 (2003).
[5] J. Adams *et al.* (STAR), Phys. Rev. Lett. **91**, 172302 (2003).
[6] S. S. Adler *et al.* (PHENIX), Phys. Rev. Lett. **91**, 072301 (2003).
[7] S. S. Adler *et al.* (PHENIX), Phys. Rev. C **69**, 034910 (2004).
[8] B. B. Back *et al.* (PHOBOS), Phys. Lett. **B578**, 297 (2004).
[9] I. Arsene *et al.* (BRAHMS), Phys. Rev. Lett. **91**, 072305 (2003).
[10] S. S. Adler *et al.* (PHENIX), Phys. Rev. Lett. **91**, 072303 (2003).
[11] J. Adams *et al.* (STAR), Phys. Rev. Lett. **91**, 072304 (2003).
[12] B. B. Back *et al.* (PHOBOS), Phys. Rev. Lett. **91**, 072302 (2003).
[13] S. S. Adler *et al.* (PHENIX), Phys. Rev. Lett. **96**, 202301 (2006).
[14] S. S. Adler *et al.* (PHENIX), Phys. Rev. Lett. **94**, 232301 (2005).
[15] C. Adler *et al.* (STAR), Phys. Rev. Lett. **90**, 032301 (2003).
[16] X.-N. Wang and M. Gyulassy, Phys. Rev. Lett. **68**, 1480 (1992).
[17] S. A. Bass *et al.*, Nucl. Phys. **A661**, 205 (1999).
[18] M. Gyulassy, I. Vitev, X.-N. Wang, and B.-W. Zhang, *Quark Gluon Plasma*, Vol. 3 (World Scientific, Singapore, 2003).
[19] A. Kovner and U. A. Wiedemann, *Quark Gluon Plasma*, Vol. 3 (World Scientific, Singapore, 2003).
[20] I. Vitev and M. Gyulassy, Phys. Rev. Lett. **89**, 252301 (2002).
[21] E. Wang and X.-N. Wang, Phys. Rev. Lett. **89**, 162301 (2002).
[22] K. J. Eskola, H. Honkanen, C. A. Salgado, and U. A. Wiedemann, Nucl. Phys. **A747**, 511 (2005).
[23] M. Gyulassy and L. McLerran, Nucl. Phys. **A750**, 30 (2005).
[24] X.-N. Wang, Nucl. Phys. **A750**, 98 (2005).
[25] P. Aurenche, F. Gelis, and H. Zaraket, Phys. Rev. D **62**, 096012 (2000).
[26] M. Arneodo, Phys. Rep. **240**, 301 (1994).
[27] R. Baier, D. Schiff, and B. G. Zakharov, Annu. Rev. Nucl. Part. Sci. **50**, 37 (2000).
[28] M. Gyulassy, P. Levai, and I. Vitev, Phys. Lett. **B538**, 282 (2002).
[29] A. Drees, H. Feng, and J. Jia, Phys. Rev. C **71**, 034909 (2005).
[30] M. Gyulassy, I. Vitev, and X. N. Wang, Phys. Rev. Lett. **86**, 2537 (2001).
[31] M. Gyulassy, I. Vitev, X.-N. Wang, and P. Huovinen, Phys. Lett. **B526**, 301 (2002).

[32] E. V. Shuryak, Phys. Rev. C **66**, 027902 (2002).

[33] B. Muller, Phys. Rev. C **67**, 061901(R) (2003).

[34] S. S. Adler *et al.* (PHENIX), Phys. Rev. Lett. **96**, 032302 (2006).

[35] K. Adcox *et al.* (PHENIX), Nucl. Instrum. Methods A **499**, 469 (2003).

[36] H. Hahn *et al.*, Nucl. Instrum. Methods A **499**, 245 (2003).

[37] L. Aphecetche *et al.* (PHENIX), Nucl. Instrum. Methods A **499**, 521 (2003).

[38] M. Allen *et al.* (PHENIX), Nucl. Instrum. Methods A **499**, 549 (2003).

[39] C. Adler *et al.*, Nucl. Instrum. Methods A **470**, 488 (2001).

[40] S. S. Adler *et al.* (PHENIX), Nucl. Instrum. Methods A **499**, 560 (2003).

[41] K. Adcox *et al.* (PHENIX), Phys. Rev. Lett. **86**, 3500 (2001).

[42] S. S. Adler *et al.* (PHENIX), Phys. Rev. Lett. **91**, 182301 (2003).

[43] S. S. Adler *et al.* (PHENIX), Phys. Rev. C **72**, 024901 (2005).

[44] A. M. Poskanzer and S. A. Voloshin, Phys. Rev. C **58**, 1671 (1998).

[45] J. Jia *et al.* (PHENIX), Nucl. Phys. **A783**, 501c (2007).

[46] S. S. Adler *et al.* (PHENIX), Phys. Rev. Lett. **91**, 241803 (2003).

[47] S. S. Adler *et al.* (PHENIX), Phys. Rev. Lett. **93**, 202002 (2004).

[48] T. Sjostrand *et al.*, Comput. Phys. Commun. **135**, 238 (2001).

[49] G. D. Lafferty and T. R. Wyatt, Nucl. Instrum. Methods A **355**, 541 (1995).

[50] S. Eidelman *et al.* (Particle Data Group), Phys. Lett. **B592**, 1 (2004).

[51] M. L. Miller, K. Reygers, S. J. Sanders, and P. Steinberg, to appear in Annu. Rev. Nucl. Part. Sci. **57**, 205 (2007).

[52] K. Adcox *et al.* (PHENIX Collaboration), Nucl. Phys. **A757**, 184 (2005).

[53] S. S. Adler *et al.* (PHENIX), Phys. Rev. Lett. **98**, 172302 (2007).

[54] I. Vitev, Phys. Lett. **B639**, 38 (2006).

[55] A. Dainese, C. Loizides, and G. Paic, Acta Phys. Hung. **A27**, 245 (2006).

[56] M. Jacob and P. V. Landshoff, Phys. Rep. **48**, 285 (1978).

[57] A. Dainese, C. Loizides, and G. Paic, Eur. Phys. J. C **38**, 461 (2005).

[58] V. S. Pantuev, JETP Lett. **85**, 104 (2005).

[59] A. Adil and M. Gyulassy, Phys. Rev. C **72**, 034907 (2005).

[60] E. V. Shuryak and I. Zahed, Phys. Rev. C **70**, 021901(R) (2004).